Investigating the Relationship between Polarimetric Radar Signatures of Hydrometeor Size Sorting and Tornadic Potential in Simulated Supercells

SCOTT D. LOEFFLER,[a,c] MATTHEW R. KUMJIAN,[a] PAUL M. MARKOWSKI,[a] BRICE E. COFFER,[b] AND MATTHEW D. PARKER[b]

[a] *Department of Meteorology and Atmospheric Science, The Pennsylvania State University, University Park, Pennsylvania*
[b] *Department of Marine, Earth, and Atmospheric Sciences, North Carolina State University, Raleigh, North Carolina*
[c] *Department of Ocean and Atmospheric Sciences, U.S. Naval Academy, Annapolis, Maryland*

(Manuscript received 19 August 2022, in final form 11 April 2023, accepted 21 April 2023)

ABSTRACT: The national upgrade of the operational weather radar network to include polarimetric capabilities has led to numerous studies focusing on polarimetric radar signatures commonly observed in supercells. One such signature is the horizontal separation of regions of enhanced differential reflectivity (Z_{DR}) and specific differential phase (K_{DP}) values due to hydrometeor size sorting. Recent observational studies have shown that the orientation of this separation tends to be more perpendicular to storm motion in supercells that produce tornadoes. Although this finding has potential operational utility, the physical relationship between this observed radar signature and tornadic potential is not known. This study uses an ensemble of supercell simulations initialized with tornadic and nontornadic environments to investigate this connection. The tendency for tornadic supercells to have a more perpendicular separation orientation was reproduced, although to a lesser degree. This difference in orientation angles was caused by stronger rearward storm-relative flow in the nontornadic supercells, leading to a rearward shift of precipitation and, therefore, the enhanced K_{DP} region within the supercell. Further, this resulted in an unfavorable rearward shift of the negative buoyancy region, which led to an order of magnitude less baroclinic generation of circulation in the nontornadic simulations compared to tornadic simulations.

KEYWORDS: Tornadogenesis; Supercells; Radars/Radar observations; Cloud resolving models

1. Introduction

Supercell thunderstorms are responsible for producing a large majority of violent tornadoes, as well as tornado damage, injuries, and fatalities (e.g., Brotzge et al. 2013). Because of this, the study of supercell and tornado dynamics and environments conducive to their formation has been a dedicated area of research for several decades. The dedicated effort—along with advancements in technological capabilities—has allowed meteorologists to forecast environments favorable for supercell and tornado formation with confidence (e.g., Coniglio 2012; Gallo et al. 2018). Although supercell tornadoes are associated with better warning performance compared to nonsupercell tornadoes (Brotzge et al. 2013; Anderson-Frey et al. 2016), it remains a challenge to assess the tornadic potential of an individual supercell on the time scale of minutes to hours. Further, a majority of supercells do not produce any tornadoes (Trapp et al. 2005). Therefore, it is critical to elucidate and investigate differences between tornadic (TOR) and nontornadic (NonTOR) supercells.

Several past studies have focused attention on highlighting differences between the environments of TOR and NonTOR supercells (e.g., Rasmussen and Blanchard 1998; Thompson et al. 2003, 2012; Anderson-Frey et al. 2016, 2019). Unfortunately, there is a great deal of overlap between the weakly tornadic (EF0 and EF1 ratings) and nontornadic distributions of the relevant environmental parameters, such as lifted condensation level (LCL), convective available potential energy (CAPE), vertical wind shear, and storm-relative helicity (SRH; Davies-Jones 1984). Dedicated field campaigns, such as the second Verification of the Origins of Rotation in Tornadoes Experiment (VORTEX2; Wurman et al. 2012), have provided an abundance of observations of tornadic supercells (e.g., Wakimoto et al. 2012; Markowski et al. 2012a,b; Kosiba et al. 2013; Tanamachi et al. 2013; Weiss et al. 2015) and nontornadic supercells (e.g., Skinner et al. 2014; Murdzek et al. 2020), facilitating comparisons between tornadic and nontornadic supercells (Klees et al. 2016). In the past decade, numerical simulation studies have allowed researchers to investigate numerous aspects of the tornadogenesis process in supercells (e.g., Markowski and Richardson 2014, 2017; Orf et al. 2017; Coffer and Parker 2017, 2018; Coffer et al. 2017). Unfortunately, dedicated field observations and high-resolution cloud model simulations are not consistently available to operational forecasters in a tornado warning situation. Thus, there is great value in determining differences between TOR and NonTOR supercells that have operational utility.

An investigative tool that is routinely available to operational forecasters is weather radar. As such, uncovering differences between TOR and NonTOR supercells in radar data would have significant operational utility. Conventional radar variables that have been extensively used are the radar reflectivity factor at horizontal polarization (Z_H) and Doppler velocity. The latter is a popular radar product for interrogating potentially tornadic storms, owing to its ability to reveal azimuthal shear associated with the mesocyclone. However, a small percentage (as low as 3%) of radar-detected mesocyclones are associated with tornadoes (Jones et al. 2004). Additionally, nontornadic mesocyclones can still display a significant

Corresponding author: Scott D. Loeffler, loeffler@usna.edu

DOI: 10.1175/MWR-D-22-0228.1

degree of azimuthal shear (Trapp 1999). Because of this, issuing tornado warnings based solely on Doppler velocity data is a main contributor to the currently high false alarm ratios and warning performance (Brooks and Correia 2018).

For almost a decade, the operational Weather Surveillance Radar 1988-Doppler (WSR-88D) network has had dual-polarization, or polarimetric, capabilities (Doviak et al. 2000). Two of the polarimetric radar variables that are of particular interest in this study are differential reflectivity (Z_{DR}) and specific differential phase (K_{DP}). Differential reflectivity, introduced by Seliga and Bringi (1976, 1978), is the difference between the logarithmic radar reflectivity factors at horizontal and vertical polarizations (i.e., $Z_{DR} = Z_H - Z_V$). For hydrometeors small compared to the radar wavelength with their major axis oriented horizontally (e.g., oblate raindrops), Z_{DR} is positive ($Z_H > Z_V$). Because drops become more oblate as they grow larger (e.g., Brandes et al. 2002; Thurai and Bringi 2005; Thurai et al. 2009), Z_{DR} can also be used to assess the Z_H-weighted mean drop size: large Z_{DR} values can indicate the presence of large raindrops. Specific differential phase (K_{DP}) is a measure of the differential phase shift per unit distance (° km^{-1}) along the radar signal propagation direction and is nearly linearly related to the rainfall rate (Sachidananda and Zrnić 1986); thus, large K_{DP} values are usually located in regions of heavy rain and large liquid water content, which could include large amounts of small melting hail (Kumjian et al. 2019a). The K_{DP} is more closely related to the mass of the raindrops and less sensitive to median drop size compared to Z_H and Z_{DR}: it is proportional to the approximately fourth to fifth moment of the drop size distribution (DSD; Sachidananda and Zrnić 1986; Kumjian et al. 2019b). Drops still need to be large enough to have some measure of "oblateness" for there to be a differential phase shift; K_{DP} will be less affected by the presence of small, quasi-spherical drops. For a more extensive review, the reader is directed to the books by Doviak and Zrnić (1993), Rauber and Nesbitt (2018), Ryzhkov and Zrnic (2019), and the review series by Kumjian (2013a,b,c).

Several different polarimetric radar signatures have been repeatedly observed in supercells (e.g., Kumjian and Ryzhkov 2008; Van Den Broeke et al. 2008; Snyder et al. 2013; Kumjian 2013b). One of these common signatures is a region of increased Z_{DR} values collocated with the Z_H gradient along the inflow edge of the forward flank, called the "Z_{DR} arc" (Kumjian and Ryzhkov 2008). Additionally, there is commonly a region of increased K_{DP} values located farther into the forward flank and collocated with the precipitation core, called the "K_{DP} foot" (Romine et al. 2008). These two regions are horizontally separated due to hydrometeor size sorting (Kumjian and Ryzhkov 2009; Dawson et al. 2014).

Hydrometeor size sorting results from the variation of hydrometeor terminal velocity with size. The terminal velocity of raindrops increases with increasing raindrop size (e.g., Gunn and Kinzer 1949; Foote and du Toit 1969; Beard 1976; Brandes et al. 2002). As such, larger drops fall through a given layer of the atmosphere quicker and, therefore, spend less time in the layer compared to smaller drops. The sorting layer is defined as the layer over which the storm-relative winds can advect hydrometeors. If there are nonzero storm-relative winds in the layer, this size sorting can be maintained (Kumjian and Ryzhkov 2012; Dawson et al. 2015), with smaller drops being advected larger distances compared to larger drops. This leads to a horizontal separation of drops by size at the bottom of the sorting layer. Most of the liquid precipitation mass and highest number concentrations will come from smaller to more medium size raindrops, indicating that the region of relatively small drops will be characterized by enhanced K_{DP} values. On the other hand, the region of relatively large drops will be associated with enhanced Z_{DR} values. Thus, a layer with nonzero storm-relative winds and subsequent size sorting has created a horizontal separation between regions of enhanced K_{DP} and Z_{DR}.

Enhanced K_{DP} values indicate regions of increased hydrometeor mass that can subsequently melt or evaporate to generate negative buoyancy (along with precipitation loading), which is relevant for tornadogenesis (e.g., Markowski and Richardson 2014, 2017). Because these polarimetric radar signatures are readily observable and are also associated with processes that play a role in tornadogenesis, there is potential that this signature could show differences between TOR and NonTOR supercells, with important operational implications. The theoretical relationship between this Z_{DR}–K_{DP} separation and the storm-relative winds was analyzed by Loeffler and Kumjian (2020), who used a simple idealized size sorting model similar to that of Dawson et al. (2015). Their results showed that the separation distance and direction between the two enhancement regions was highly correlated to the mean storm-relative wind magnitude and direction in the sorting layer, respectively. Additionally, their study showed that larger SRH values in the sorting layer were associated with larger separation distances and separation directions that were more perpendicular to the shear vector in the sorting layer.

Complementing this past idealized work, several studies have analyzed this Z_{DR}–K_{DP} separation in observed storms. Crowe et al. (2012) studied the separation between enhanced Z_{DR} and K_{DP} regions in different convective modes in the southeastern United States. They found that, although both TOR and NonTOR storms tended to have the two enhanced regions overlapping, TOR storms tended to show greater separation between the two enhanced regions. However, most of the analysis was qualitative and was performed on a relatively small sample of storms (six storms). Martinaitis (2017) analyzed this separation, also in a qualitative manner, as a part of the author's radar analysis of convection associated with landfalling tropical systems in Florida. When analyzing tornado-warned circulations, the author was unable to find any significant differences between TOR and NonTOR storms. Jurewicz and Gitro (2014) assessed this separation quantitatively in supercells, and found that TOR supercells tended to have greater separation distances compared to NonTOR supercells. However, their use of point max values made their measurements susceptible to radar noise.

Loeffler and Kumjian (2018) defined the "separation vector," which comprises the separation distance (taken from K_{DP} centroid toward Z_{DR} centroid) and the orientation relative (degrees clockwise) to storm motion between the enhanced Z_{DR}

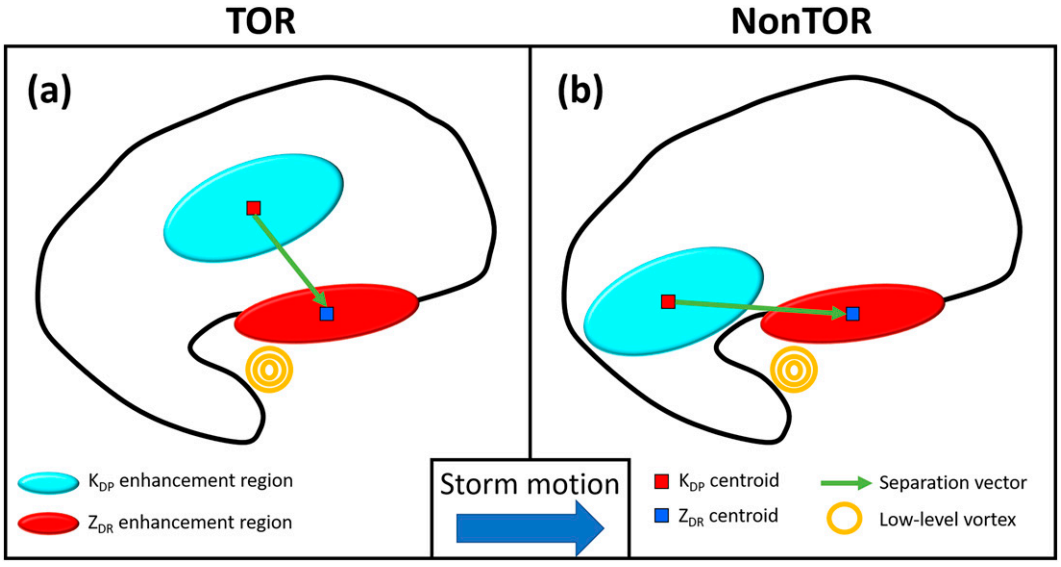

FIG. 1. Schematic showing how a rearward shift in the K_{DP} enhancement region when going from a (a) TOR supercell to a (b) NonTOR supercell could be detrimental for tornadogenesis. The K_{DP} and Z_{DR} enhancement regions are indicated by light blue and red ovals, respectively. The K_{DP} and Z_{DR} centroids are indicated by red and blue squares, respectively. Green arrows represent the separation vectors, and the orange circles represent the location of the low-level vortex. Black contours represent the Z_H outline of the supercell.

and K_{DP} regions, to analyze 30 nonsupercellular TOR storms. They showed that the separation distances tended to peak and separation orientations tended to become closer to 90° around the time of the reported tornado. A follow-up study by Loeffler et al. (2020) analyzed the separation vector in 63 TOR and 53 NonTOR supercells. Their results showed that, although separation distances were similar, TOR supercells tended to have separation vectors close to perpendicular to storm motion, whereas NonTOR supercells tended to have separation vectors closer to parallel to storm motion. This difference in orientation angles between TOR and NonTOR supercells has been corroborated by Homeyer et al. (2020) and Wilson and Van Den Broeke (2022). Both of these studies analyzed independent datasets of a large number of supercells using different methods and found that TOR supercells had Z_{DR}–K_{DP} separation vectors that were more perpendicular to storm motion than those in NonTOR supercells.

Although recent studies have identified this key observational difference in separation orientation angles between TOR and NonTOR supercells, we need to understand what this observed difference means physically and how it potentially relates to tornadogenesis. In this study, we will analyze the ensemble of TOR and NonTOR cloud model simulations from Coffer et al. (2017) to make connections between this observed radar signature and tornadogenesis processes. Their simulations, initialized with composite TOR and NonTOR near-storm environments, highlighted the role of increased environmental low-level streamwise vorticity. Supercells initialized with the composite TOR environments ingested more streamwise vorticity and subsequently developed stronger low-level [≈1 km above ground level (AGL)] circulation, allowing for increased dynamic lifting and vortex stretching.

The K_{DP} region is of particular interest, due to its relationship to precipitation mass, in generating hypotheses for the connection between this polarimetric size sorting signature and tornadogenesis processes. Markowski and Richardson (2017) showed how the relative location of a heat sink to a heat source (analogous to an updraft) could significantly change the near-surface vertical vorticity. This heat sink is analogous to the negative buoyancy generated by the main region of precipitation in the supercell forward flank and, therefore, could be collocated with the K_{DP} enhancement region. Additionally, Gray and Frame (2021) showed that the storm-relative location for outflow surges was spatially related to the location of the greatest precipitation loading, presumably also collocated with the K_{DP} enhancement region. Therefore, this relative location of the K_{DP} enhancement region within the supercell is at the foundation of our hypotheses to be tested in this study. A multipart hypothesis that could explain how the observed polarimetric radar signature relates to tornadogenesis, which will be tested in this study, is presented below. H1 and H2 are motivated by previous observational work showing a more parallel separation angle in nontornadic supercells and provide a potential explanation. H3 and H4 are attempts to connect this difference in observations with processes related to tornadogenesis, specifically how this shift in K_{DP} could be detrimental to tornadogenesis. A schematic of this is shown in Fig. 1.

- H1: The K_{DP} enhancement region is shifted farther rearward, in a storm-relative sense, in NonTOR supercells compared to TOR supercells.
- H2: This rearward shift of the K_{DP} enhancement region in NonTOR supercells leads to separation angles more parallel to storm motion.

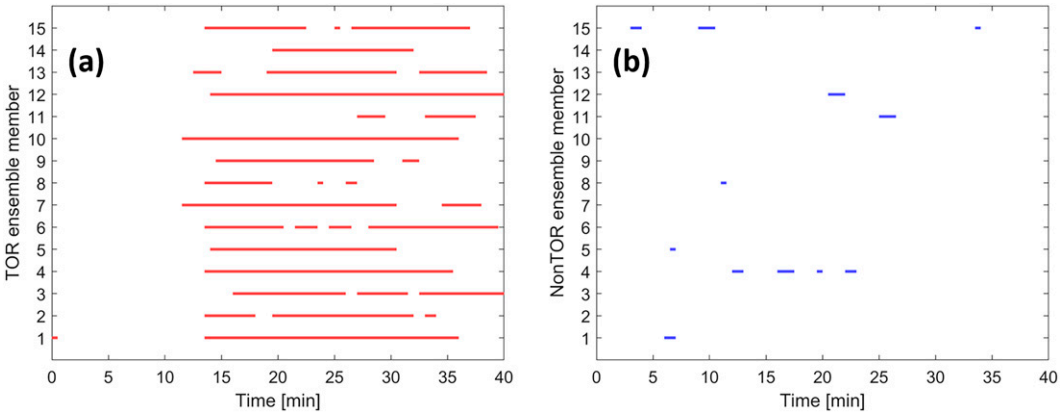

FIG. 2. Time series highlighting periods during the analysis period when surface vertical vorticity exceeds 0.4 s^{-1} and maximum surface wind speed exceeds 40 m s^{-1} for (a) TOR and (b) NonTOR ensemble members.

- H3: Negative buoyancy resulting from the increased hydrometeor mass associated with the K_{DP} enhancement region, therefore, is placed too close to the low-level updraft/near-surface vertical vorticity.
- H4: Parcels become too negatively buoyant to be lifted and/or the stronger cold pool and outflow disrupt the updraft and stretching of the near-surface vertical vorticity, such as that seen in Markowski et al. (2011) and Markowski and Richardson (2014).

2. Data and methodology

a. *Model configuration and simulations*

In this study, we use the ensemble of Cloud Model 1 (CM1; Bryan and Fritsch 2002) supercell simulations from Coffer et al. (2017). Detailed model specifications can be found in Coffer and Parker (2017) and Coffer et al. (2017), but will be reviewed here. These storms are the members of ensembles of supercells initialized with composite environments from TOR and NonTOR storms observed during the second Verification of the Origins of Rotation in Tornadoes Experiment (VORTEX2; Wurman et al. 2012; Parker 2014). For the rest of this study, we will simply refer to storms initialized with the tornadic environments as "TOR" and those initialized with the nontornadic environments as "NonTOR." It is worth noting that about 40% of the storms initialized in the NonTOR environments did produce tornadoes as defined by subjective criteria listed in Coffer et al. (2017) that needed to be met for at least two minutes. However, these tornadoes were weaker than those initialized in the TOR environments, and if the original thresholds are marginally increased (surface vertical vorticity increased from 0.3 to 0.4 s^{-1} and maximum surface wind speed increased from 35 to 40 m s^{-1}), all of the TOR ensemble members still meet the criteria for at least a 2-min period, while none of the NonTOR ensemble members do (Fig. 2). This gives us confidence that these two ensembles of simulations are different "classes" and we can group them together in our analyses moving forward. There are 15 members in both TOR and NonTOR ensembles, including a control simulation using the base-state thermodynamic and wind profiles from Coffer and Parker (2017). The NonTOR ensemble environments are not drastically different with regards to the thermodynamic and wind profiles compared to the TOR ensemble environments, a feature exploited by Coffer and Parker (2018). This provides a more stringent test of our hypotheses compared to observational work that has analyzed NonTOR supercells from a broader set of environments. (e.g., Loeffler et al. 2020). Thus, we may expect a more subtle difference between TOR and NonTOR storms.

The vertical wind profiles used for each set of the remaining 14 ensemble members have horizontal wind perturbations applied to the composite profile. These perturbations are $\leq$2 m s^{-1} in magnitude and are identical between the corresponding members of the TOR and NonTOR ensemble members. The composite TOR and NonTOR storm-relative 0–6-km hodographs (i.e., simulated storm motion is placed at the origin), along with each of their 14 ensemble members, are shown in Fig. 3. The variation of the storm-relative wind profile makes these simulations an attractive choice when considering signatures of hydrometeor size sorting. One feature that stands out is the westward bulge in the low-level (0–1 km) NonTOR hodographs compared to the TOR hodographs. This feature can be considered an enhancement of rearward low-level storm-relative winds (storm motion is approximately due east). This 0–1 km AGL portion of the wind profile was of particular interest in Coffer and Parker (2017), as they emphasized the difference between the crosswise and streamwise components of the low-level environmental horizontal vorticity evident in the NonTOR and TOR wind profiles, respectively.

The model domain moves with the storm and is 200 km × 200 km in the horizontal and extends to just over 18 km in the vertical. The horizontal grid spacing in the inner 100 km × 100 km area is 125 m, and stretches to 4.875 km at the outer boundaries of the larger 200 km × 200 km domain. Vertical grid spacing is 20 m in the lowest 300 m, starting at 10 m. Above 300 m, it stretches to 280 m at 12 km and maintains that grid spacing to the top of the domain. This results in 115 vertical levels, 31 of them contained in the lowest 1 km of the domain.

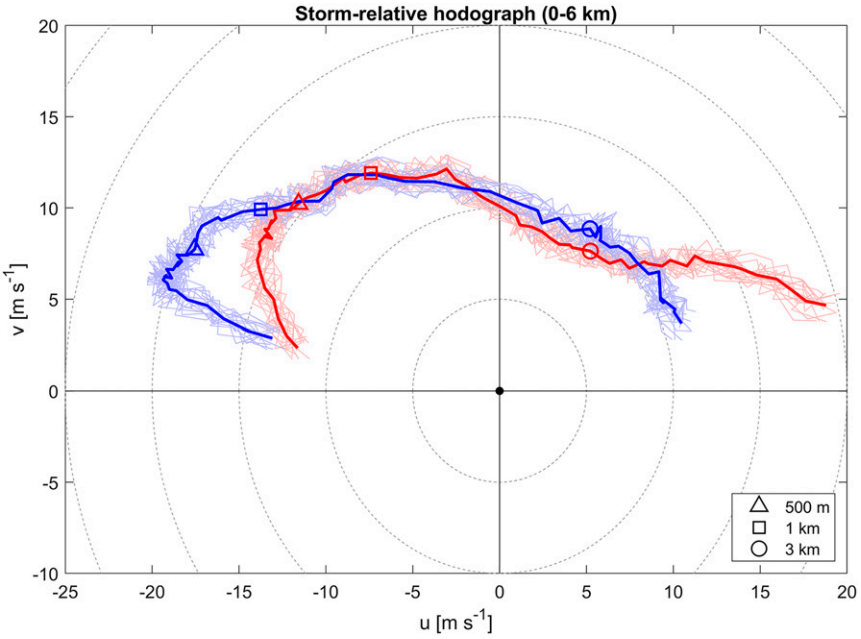

FIG. 3. Storm-relative hodographs (0–6 km AGL layer) for the TOR (red) and NonTOR (blue) ensemble members, with the thicker lines indicating the composite VORTEX2 profile and the thinner lines indicating the 14 ensemble members for each storm type. Red triangle, square, and circle markers indicate the wind at 500-m, 1-km, and 3-km heights in the TOR simulations with corresponding blue markers for the NonTOR simulations. Adapted from Coffer et al. (2017).

The NSSL two-moment bulk microphysics scheme (Ziegler 1985; Mansell 2010; Mansell et al. 2010) is used, which has been shown to produce size sorting signatures that compare well with observations (Johnson et al. 2016). In particular, the NSSL scheme has several different sedimentation treatments to help limit excessive size sorting. This study used the default setting (infall = 4), which was shown to provide the best results in Mansell (2010). This parameterization assumes a three-parameter gamma distribution for hydrometeor size distributions, with the shape parameter set to zero for rain and graupel and set to two for hail. For each simulation, model output is saved every minute for a 40-min period. For the TOR storms, the 40–80-min time period is chosen to capture when tornadolike vortices are present. The NonTOR storm data are saved for the 50–90-min period, subjectively chosen due to the NonTOR simulations taking slightly longer to initiate storms and for those storms to organize.

b. Separation vector calculations

For a detailed description of the polarimetric radar forward operator implemented in this study, the reader is referred to the appendix. The forward operator produces realistic K_{DP} enhancement regions that agree with observations, with these regions located farther into the forward flank (e.g., Romine et al. 2008; Homeyer et al. 2020) and correlating well with the bulk of the liquid precipitation mass (shown in section 3c). On the other hand, the forward operator struggles to produce a realistic Z_{DR} arc. Although the forward operator produces a hail Z_{DR} field (Fig. 4c) consistent with physical expectations, the rain Z_{DR} field does not agree well with observations. In observed supercells, the Z_{DR} arc is characterized by enhanced Z_{DR} values along the inflow edge of the forward flank along the gradient in Z_H (Kumjian and Ryzhkov 2008). However, the simulated rain Z_{DR} field shows enhanced values pushed farther into the forward flank, away from the gradient in Z_H (Fig. 4a). To investigate why, we look at the mass-weighted mean drop diameter $\overline{D}_m = M_4/M_3$, where M_3 and M_4 are the third and fourth moments of the rain DSD, respectively. Because Z_{DR} provides a good estimate of median drop size, the fields of Z_{DR} and $\overline{D}_m$ (Fig. 4b) look remarkably similar, indicating that the radar forward operator is behaving as expected by producing greater Z_{DR} values in locations of increased $\overline{D}_m$. In contrast to observed supercells, however, there is no pronounced region of bigger drops evident along the forward-flank Z_H gradient, which indicates the discrepancy lies with the model microphysics and not with the forward operator. The NSSL two-moment microphysics scheme has a sedimentation treatment that helps reduce excessive size sorting (Mansell 2010), which is a common issue with two-moment bulk microphysics schemes (Kumjian and Ryzhkov 2012). However, it seems that the microphysics scheme was too aggressive in suppressing excessive size sorting. The other sedimentation treatments in the NSSL scheme were also tested and did not yield better results. This overcorrection should be explored further, but is beyond the scope and aim of this study.

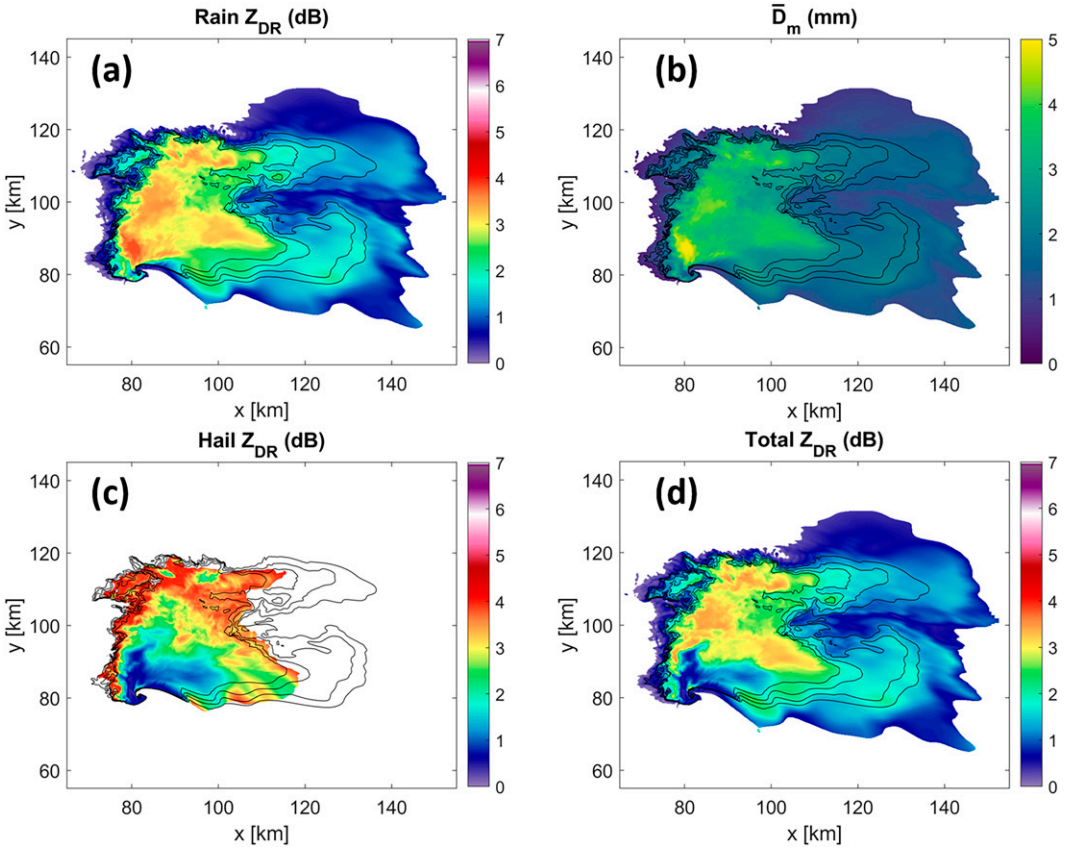

FIG. 4. Simulated near-surface (a) rain Z_{DR} (dB), (b) mass-weighted mean drop diameter (mm), (c) hail Z_{DR}, and (d) total Z_{DR} for a TOR member. Contours of Z_H for 25, 30, 35, and 40 dBZ are overlaid in black in each panel.

Owing to the lack of a realistic Z_{DR} arc, we need to determine a proxy for the Z_{DR} arc for use in calculating the separation vector. Because the inflow edge of the forward flank is oriented roughly west–east in most of the simulations, we approximate the Z_H gradient by calculating $\Delta Z_H/\Delta y$. The resulting field is rather noisy (Fig. 5a), so we smooth this field by using a 50-grid window moving average in the y direction (Fig. 5b). The Z_H gradient values are enhanced in a region along the inflow edge of the forward flank, as expected. Given that the Z_{DR} arc is observed in nature along this gradient (see Fig. 5 in Kumjian and Ryzhkov 2008), the smoothed Z_H gradient is what we use as a proxy for calculating the separation vector. The Z_{DR} centroid in past observational work (Loeffler et al. 2020) is often found along the Z_H gradient (not shown here), providing confidence in utilizing this proxy. Limited comparisons of these two methods on observational data

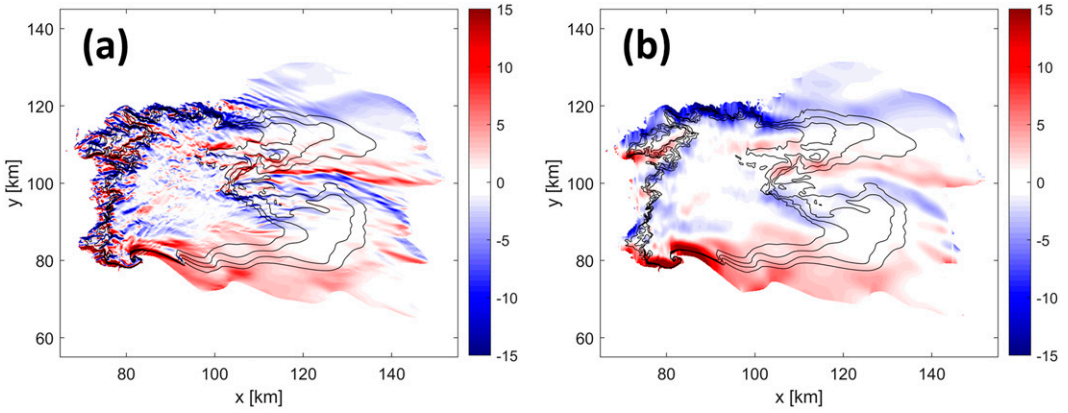

FIG. 5. As in Fig. 4 but for the (a) raw and (b) smoothed Z_H gradient field (dB km^{-1}).

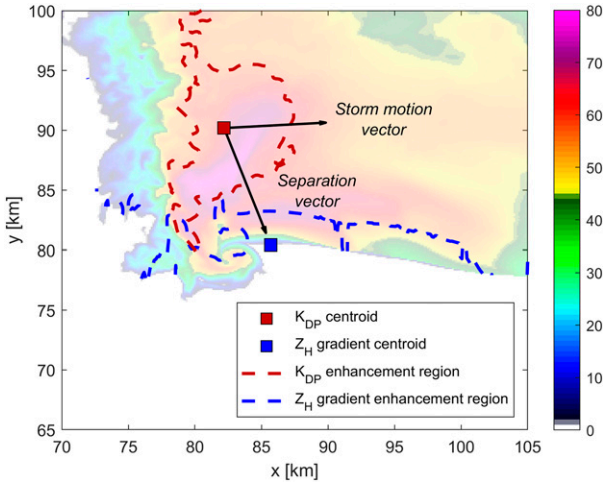

FIG. 6. Near-surface Z_H (dBZ) from a TOR member with K_{DP} and Z_H gradient centroid markers (red and blue squares, respectively) and enhancement regions (red and blue contours, respectively) overlaid. Separation and storm motion vectors are also overlaid (black arrows).

show that the Z_H gradient centroids might be shifted along the reflectivity gradient closer to the hook echo, leading to smaller separation distances and larger separation angles. However, we expect that this shift is consistent across TOR and NonTOR cases. Thus, using the Z_H gradient centroid instead of the Z_{DR} enhancement region centroid preserves the key differences between the two supercell types (whereas caution is warranted in comparing the absolute values of the separation vector between these two methods). This has potential utility for radars without polarimetric capabilities that wish to analyze this signature. Although reproducing a realistic Z_{DR} arc is desired for assessing this polarimetric size sorting signature, our hypothesis is more focused on the relative location of the K_{DP} enhancement region and its effects on tornadogenesis. Therefore, we have confidence in our results moving forward.

The calculation of the separation vector here is similar to that done in previous observational work (Loeffler and Kumjian 2018; Loeffler et al. 2020). Briefly, a region of interest is indicated by an "analysis box" to avoid sampling entire fields, and only gates within the analysis box are considered. This method uses an "adaptive threshold" to identify Z_{DR} and K_{DP} enhancement regions. Rather than using subjective Z_{DR} and K_{DP} thresholds, a gate threshold is used that defines the minimum number of gates that can comprise an enhancement region. The algorithm then finds the largest Z_{DR} and K_{DP} threshold value that produces an enhancement region of at least that many gates. All the radar gates within the analysis box that have a Z_{DR} or K_{DP} value greater than the objectively chosen threshold determine the enhancement region. Then, the centroid of the enhancement region is determined by calculating the median x and y coordinates of all the gates that comprise the enhancement region [see Fig. 2 in Loeffler and Kumjian (2018) for reference]. The separation vector points from the K_{DP} centroid toward the Z_{DR} centroid. The distance between these two centroids is the separation distance (i.e., length of the separation vector) and the angle between the separation vector and storm motion is the separation orientation (defined as degrees clockwise from storm motion).

A few adjustments to this method are made for this study. First, we use the Z_H gradient field in place of Z_{DR}, as discussed above. Second, the "adaptive thresholds" for the K_{DP} and Z_H gradient enhancement regions are chosen using increments of 0.5° km^{-1} and 1 dB km^{-1}, respectively. Instead of a gate threshold like that used in observational analysis, here we use an area threshold of 80 km^2, similar to the average Z_{DR} arc areal extent found in Van Den Broeke (2017). Because the storms are located within the inner 100 km × 100 km domain (consistent grid size), the area threshold acts in a similar manner to a gate threshold and should not alter the results. Third, the storm motion vector used is simply the motion of the domain that keeps the supercell centered. Fourth, because the supercells stay in the center of the domain and because they are rather large and isolated, we use a larger analysis box of 55 km × 55 km focused on the center of the domain, compared to the approximately 25 km × 25 km analysis boxes used in previous observational work. This larger analysis box opens the potential for separation distances to be larger on average than those seen in previous observational work. This methodology is

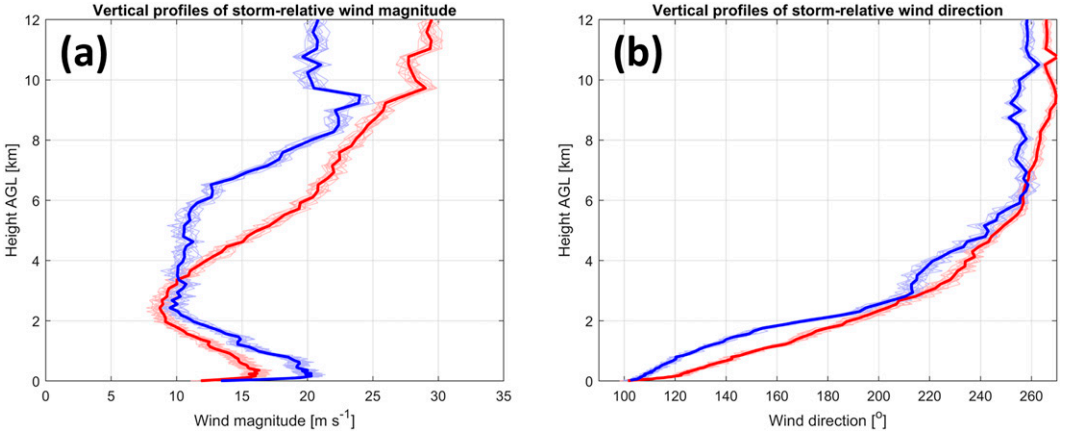

FIG. 7. Vertical profiles of storm-relative wind (a) magnitude and (b) direction. Line color and thickness is as in Fig. 3.

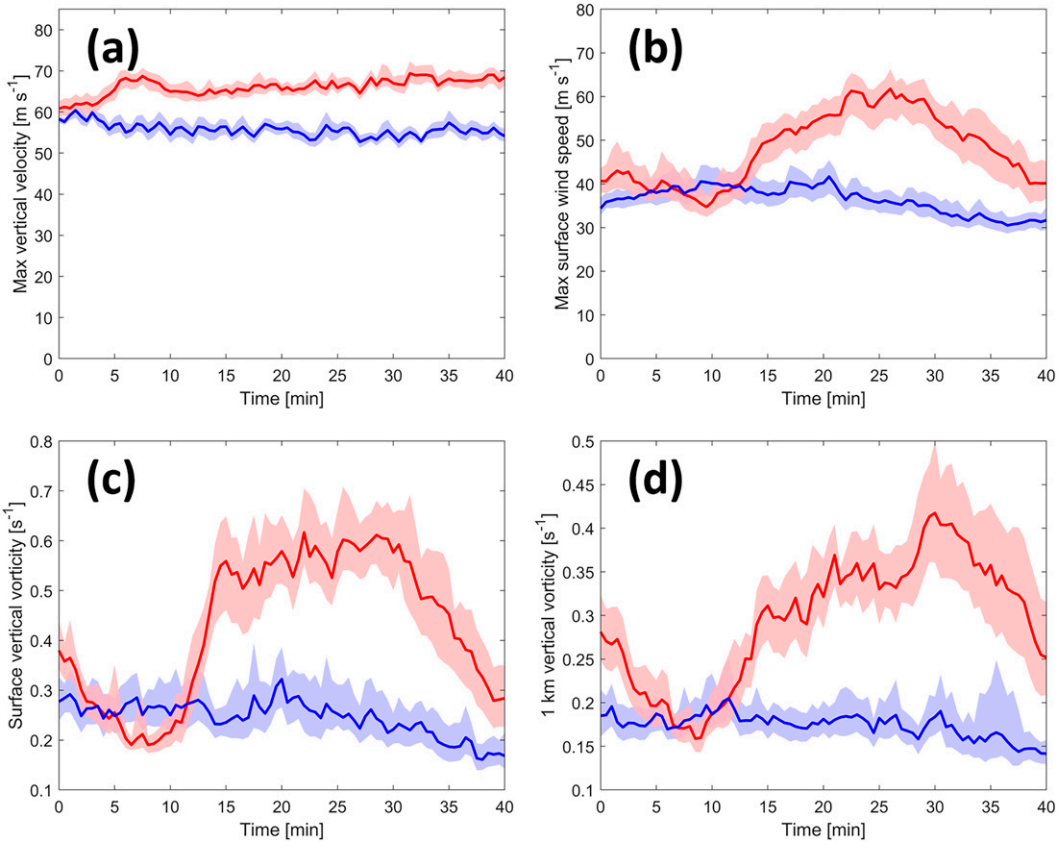

FIG. 8. Composite mean time series for TOR (red line) and NonTOR (blue line) simulations with 95% bootstrapped confidence intervals in shading for (a) maximum vertical velocity, (b) maximum surface horizontal wind speed, (c) surface vertical vorticity, and (d) 1 km AGL vertical vorticity.

applied to the K_{DP} and Z_H gradient fields at the lowest model level (10 m AGL) for calculating the separation vector. An example result from this algorithm is shown in Fig. 6.

3. Results and discussion

a. *Environmental and storm characteristics*

Figure 7 shows vertical profiles of the storm-relative wind magnitude and direction. Within the 0–2 km AGL layer, we see the NonTOR storm-relative winds maintain larger magnitudes, and that the NonTOR and TOR winds (with the exception of the very top of this layer) have an easterly component, with the NonTOR winds more backed. These indicate there is stronger westward or rearward flow at low levels in the NonTOR simulations compared to the TOR storms. At midlevels (4–6 km), the comparison in the storm-relative wind magnitude has reversed: the NonTOR winds are now weaker than the TOR winds. The wind direction in this layer for both sets of simulations is approximately southwesterly or west-southwesterly. This indicates that the NonTOR storms have environments with weaker flow to the northeast or east-northeast at midlevels compared to the TOR storms. Taken together, this suggests that hydrometeors are advected farther to the northeast away from the updraft in TOR storms and hydrometeors remain closer to the updraft in NonTOR storms.

The differing environments lead to storm structural and behavioral differences described in Coffer et al. (2017) (Fig. 8). The TOR simulations consistently maintain stronger updrafts (max w) throughout the analysis period and are statistically significantly different after approximately 5 min (Fig. 8a). The tornadic period of the simulations is well captured, with maximum wind speed (Fig. 8b) and surface vertical vorticity (Fig. 8c) noticeably increasing between 10 and 15 min and maintaining larger values between 15 and 30 min before weakening for the remainder of the analysis period. After 10–15 min, these two quantities remain statistically significantly larger for the remainder of the analysis period. A similar trend is seen for the low-level (1 km AGL) vertical vorticity (Fig. 8d).

b. *Separation vector characteristics for TOR and NonTOR simulations*

We can assess the distributions of the separation vector in the TOR and NonTOR simulations using kernel density estimates (e.g., Peel and Wilson 2008; Anderson-Frey et al. 2016). The distributions of TOR and NonTOR separation vectors across all

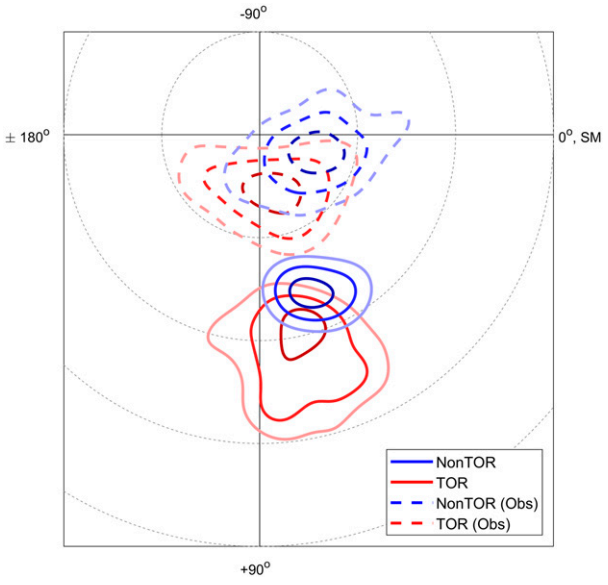

FIG. 9. Distribution of separation vectors across all times and all ensemble members. Gray dotted lines indicate separation distances in 5-km intervals. Red and blue solid contours represent 50%, 70%, and 90% of the maximum density of points for TOR and NonTOR cases, respectively. The corresponding contours for the observational data from Loeffler et al. (2020) are shown in dashed lines for reference.

cases and all times is shown in Fig. 9, with contours representing 50%, 70%, and 90% of the maximum density of observations for both supercell types. The figure is constructed such that storm motion is in the $+x$ direction, so a separation vector pointing parallel to storm motion (i.e., orientation angle of 0°) would also be directed in the $+x$ direction. Separation vectors directed in the $-y$, $+y$, and $-x$ thus correspond to orientation angles of 90°, −90°, and ±180°, respectively. Another way of interpreting this figure is that the K_{DP} centroids are placed at the origin and the contours are showing higher densities of observed Z_H gradient centroid locations relative to storm motion ($+x$ direction). The TOR supercells tend to concentrate at larger separation distances compared to NonTOR supercells, contrary to observations. Both sets of separation vectors have orientations that are closer to perpendicular, rather than parallel. However, the TOR separation vectors are closer to perpendicular to storm motion than NonTOR separation vectors, in agreement with observations (e.g., Loeffler et al. 2020; Homeyer et al. 2020).

To analyze the evolution of the separation vectors we compute composite time series of the two components of the separation vector, distance and orientation (Fig. 10). Unlike observed supercells, which exhibited similar separation distances (Loeffler et al. 2020), the simulated supercells show a distinct difference in separation distance. The TOR supercells reach significantly larger separation distances compared to the NonTOR supercells, as shown by the clear separation between the 95% bootstrapped confidence intervals, especially during the middle of the analysis period. However, the more significant result from observational studies was the differences in separation orientation between TOR and NonTOR storms. We can see in the composite time series of separation orientation angles that both sets of simulations have orientation angles closer to perpendicular than to parallel. However, the composite time series nicely illustrates the subtle difference between the TOR and NonTOR orientation angles. This figure shows that, of the two, the TOR simulations produce orientation angles that are closer to orthogonal than the NonTOR simulations, especially for the first 20–25 min of the analysis, where we can see separation between the 95% bootstrapped confidence intervals for the two simulation types. This indicates that, although the NonTOR orientation angles are farther from parallel than they are in the observed cases, the tendency for TOR cases to be more orthogonal compared to NonTOR cases is reproduced in these simulations. Further, this tendency is statistically significant and can be assessed using our current observational radar network, providing confidence for its potential utilization in operations.

c. *Storm-relative composite fields*

Being able to reproduce the polarimetric radar size sorting signature to a reasonable degree in these simulations is only an

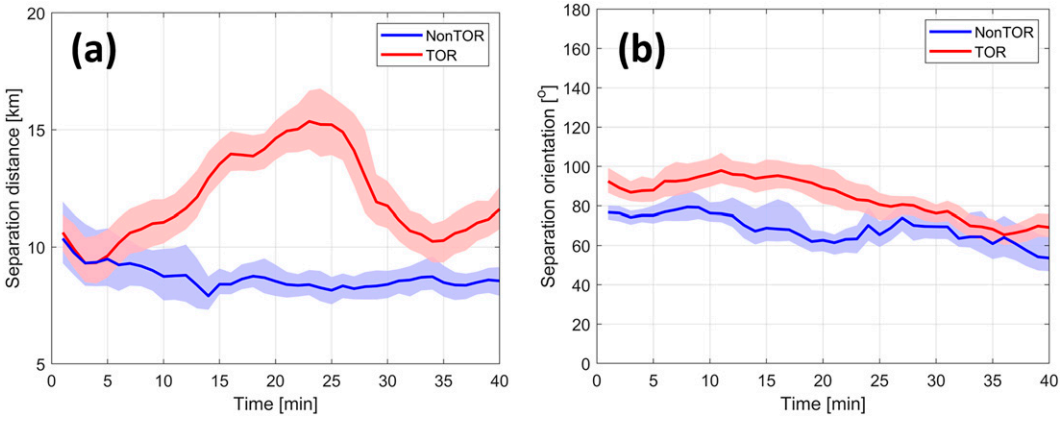

FIG. 10. Composite time series of separation (a) distance and (b) orientation relative to storm motion for TOR (red solid line) and NonTOR (blue solid line) supercell simulations. Shading for each time series represents the 95% bootstrapped confidence interval (n = 5000 samples).

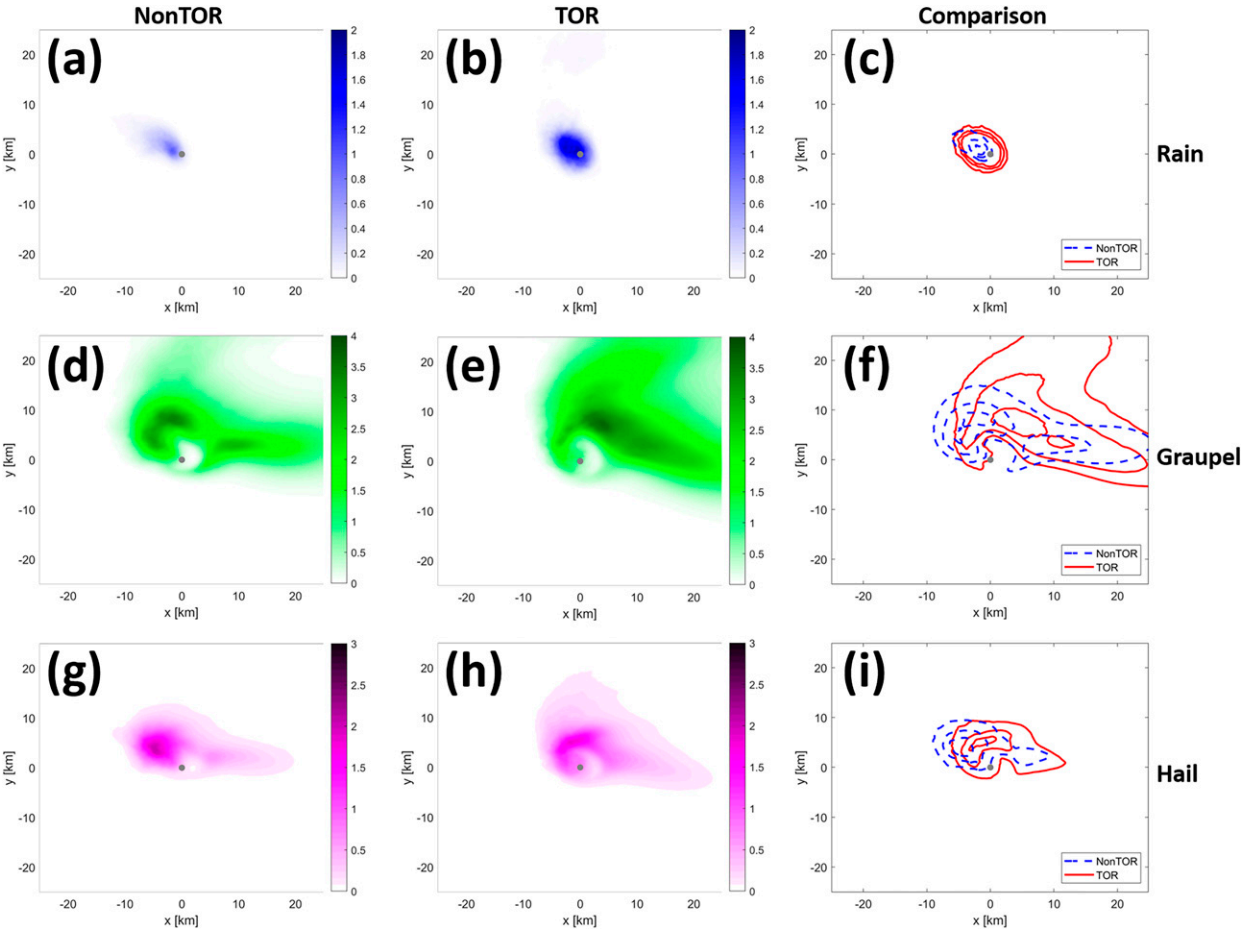

FIG. 11. Composite fields of hydrometeor mass mixing ratio (g kg^{-1}) at 6 km AGL. (a) NonTOR, (b) TOR, and (c) comparison of the two rain composite fields. NonTOR (blue dashed) and TOR (red solid) contours are shown for 0.25, 0.5, and 0.75 g kg^{-1}. (d)–(f) As in (a)–(c), but for graupel composite fields. Contours are shown for 1, 2, and 3 g kg^{-1}. (g)–(i) As in (a)–(c), but for hail composite fields. Contours are shown for 0.4, 1, and 1.6 g kg^{-1}. The gray dot represents the updraft at 5 km AGL.

initial goal of this study. The main motivation is to understand how this signature is related to the dynamics of these storms, and how it may be related to tornadogenesis. One avenue of exploring this relationship is to analyze the average kinematic and microphysical structure of the storms. We do this by using an "anchored grid" approach. First, a storm-relative anchor point is identified. Here, we use the updraft center (which is calculated as the centroid of the $w > 30$ m s^{-1} region) at 5 km AGL. Next, we take a 50 km $\times$ 50 km grid centered on this anchor point. We obtain these "anchored grids" for every model output time and composite the fields for all times across all simulations for a given storm type (TOR or NonTOR).

We assess the composite fields from the top down, emulating the path that hydrometeors take on their descent. We start at 6 km AGL where the storm-relative flow is approximately WSW for both TOR and NonTOR, but the flow is weaker for the NonTOR wind profiles compared to TOR wind profiles (cf. Fig. 7). The composite rain, graupel, and hail mass fields for TOR and NonTOR simulations are shown in Fig. 11. The left column shows the NonTOR composite, the middle column shows the TOR composite, and the right column shows a contoured comparison of the two. The top, middle, and bottom rows display the composited rain, graupel, and hail mass mixing ratio fields, respectively.

The rain composite fields for TOR and NonTOR simulations show similar locations in the center of the anchored grid for a majority of the rain mass. This is expected given that the center of the domain (gray circle) represents the midlevel updraft and liquid rain would be found in and near the updraft at 6 km as it is advected upward above the environmental 0°C level (approximately 3.5 km in these simulations) (Kumjian et al. 2014). However, the TOR composite shows noticeably greater rain mass at 6 km than the NonTOR composite, which matches well with the fact that the TOR simulations consistently maintain stronger updrafts (cf. Fig. 8a).

The graupel composite fields show more noticeable differences in the precipitation spatial distribution. The bulk of the graupel mass in the TOR composite is concentrated to the north and east of the updraft, whereas the NonTOR composite shows graupel mass concentrated more to the northwest of

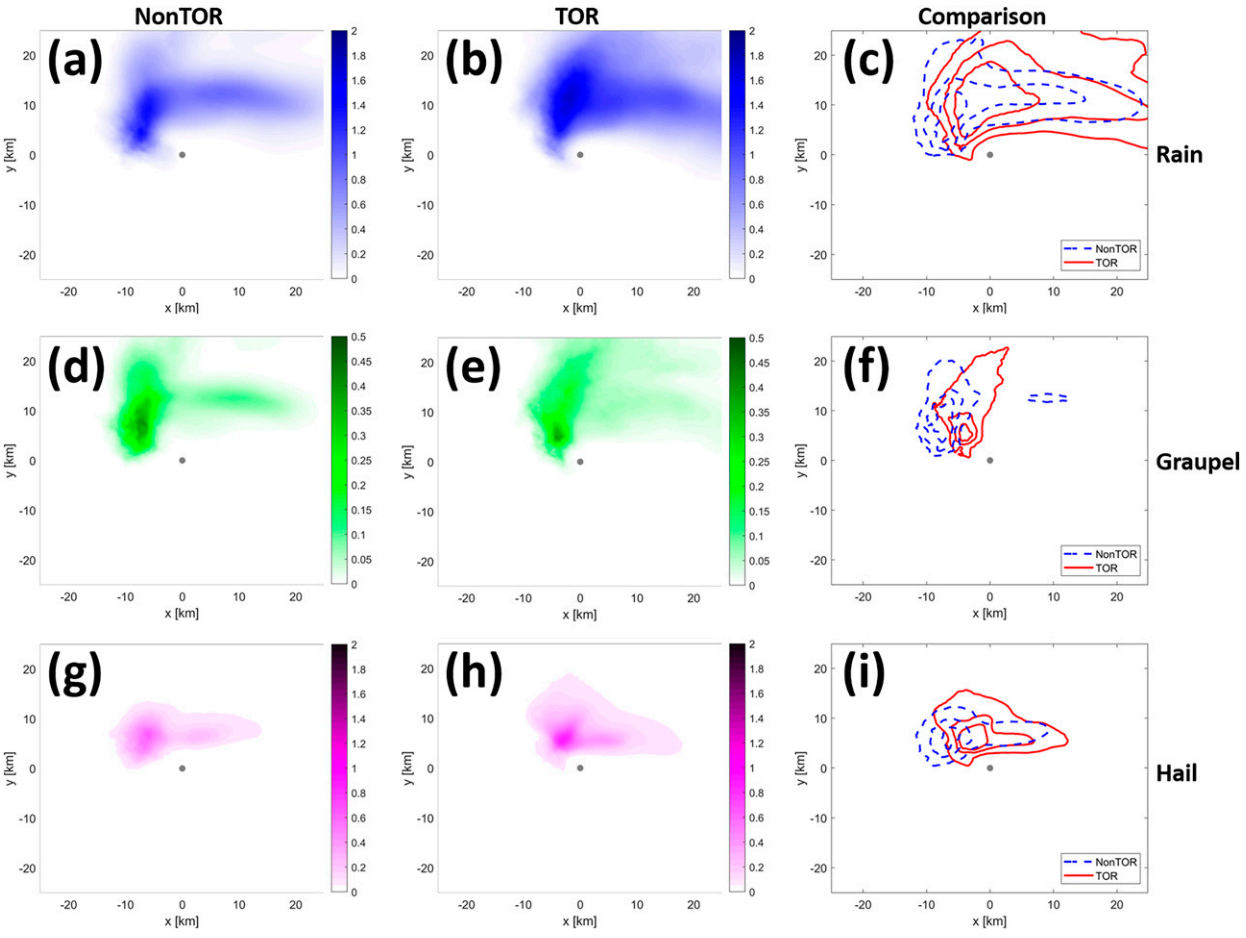

FIG. 12. As in Fig. 11, but for 1 km AGL. (c) Rain contours are shown for 0.3, 0.7, and 1.1 g kg^{-1}. (f) Graupel contours are shown for 0.1, 0.2, and 0.3 g kg^{-1}. (i) Hail contours are shown for 0.1, 0.3, and 0.5 g kg^{-1}.

the updraft, illustrating a westward/rearward shift compared to the TOR composite. The TOR composite also shows the graupel mass region extending farther toward the northeast corner of the grid. These differences in the areal graupel distribution might be explained by the differences in storm-relative flow at this height. The stronger west-southwesterly flow in the TOR wind profiles could lead to more efficient advection of graupel to the east-northeast into the forward flank compared to the weaker flow in the NonTOR profiles. The differences in the composite hail fields are more subtle. The NonTOR composite shows an increase in hail mass that is also shifted rearward compared to the TOR hail composite.

We focus next on the low-level composite fields at 1 km AGL (Fig. 12). The storm-relative wind profiles show that both sets of simulations have an easterly component and that the NonTOR profiles have stronger flow at this level. The TOR rain composite shows a slight increase in rain mass compared to the NonTOR composite. This field also shows a greater extent of the rain mass toward the northeast corner of the anchored grid, similar to the differences in the graupel field at 6 km. This implies the greater amount of graupel aloft leads to rain below after descent and melting, producing the northeastward extent of the rain field at lower levels. On the other hand, we see a rearward shift of the NonTOR rain mass due to the increased rearward storm-relative flow at low levels for the NonTOR simulations (Fig. 12c).

There are subtle differences between the TOR and NonTOR composite fields of both graupel and hail magnitude. There is a slightly larger graupel mass maximum in the NonTOR composite, whereas the hail mass maximum in the TOR composite has an increased magnitude. However, the more noticeable differences between TOR and NonTOR composites are seen in the locations of these maxima relative to the updraft (Figs. 12f,i). For both graupel and hail, we see the bulk of the mass concentrated further rearward in the NonTOR composite compared to the TOR composite. Once again, this rearward shift is due to the stronger rearward storm-relative flow at this level in the NonTOR profiles combined with the weaker flow aloft being less efficient at advecting these hydrometeors north and eastward.

The composite fields at the lowest model level, 10 m AGL (Fig. 13), show similar trends to those seen at 1 km AGL. Once again we see similar magnitudes in the rain mass maxima between the two composites, but the TOR composite

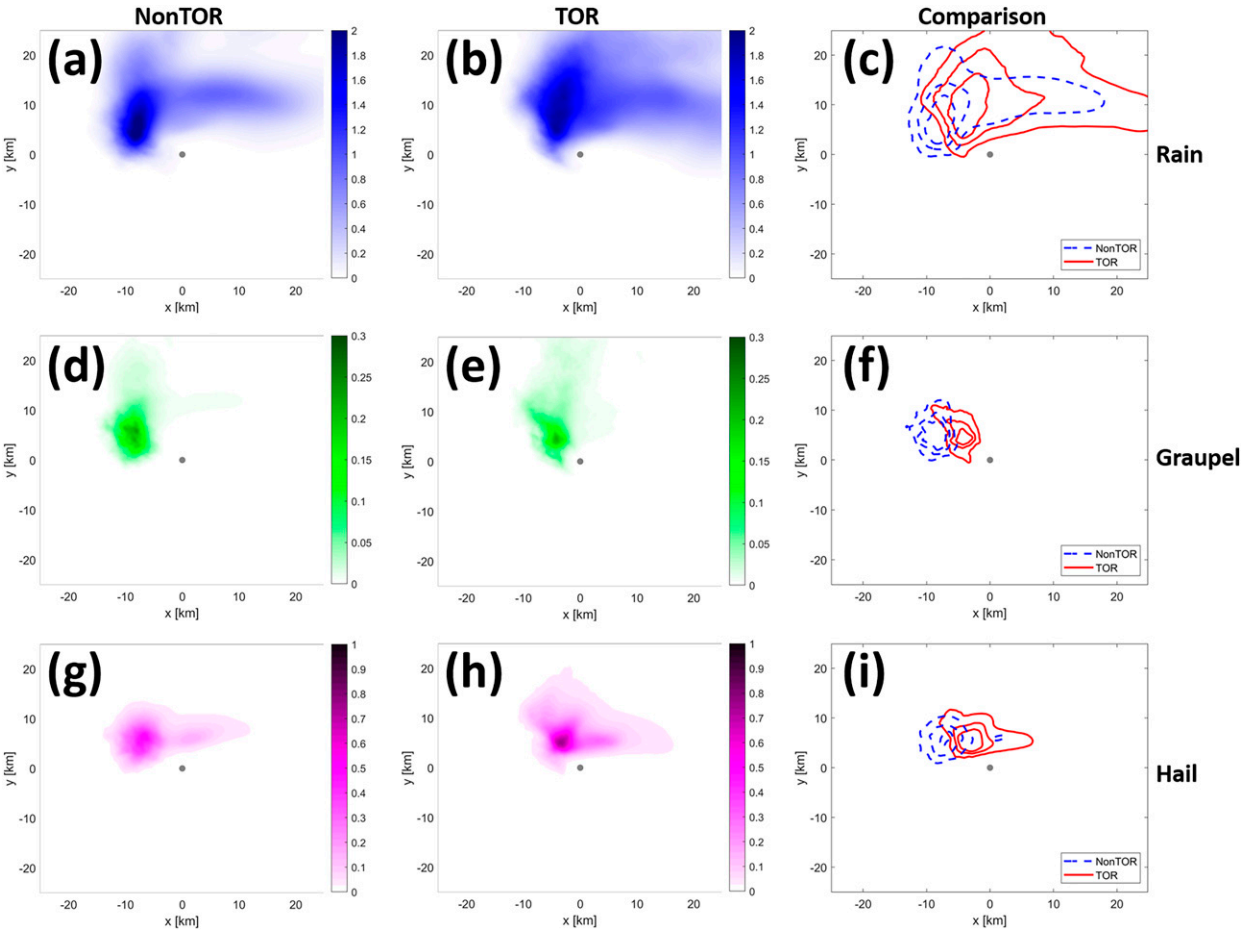

FIG. 13. As in Fig. 11, but for the near-surface level. (c) Rain contours are shown for 0.5, 1, and 1.5 g kg^{-1}. (f) Graupel contours are shown for 0.05, 0.1, and 0.15 g kg^{-1}. (i) Hail contours are shown for 0.15, 0.3, and 0.45 g kg^{-1}.

rain field extends farther to the northeast and the NonTOR composite is shifted more rearward. The TOR hail mass composite shows an increased magnitude compared to the NonTOR composite, whereas the NonTOR graupel mass composite shows a slightly larger enhanced region than seen in the TOR composite (Fig. 13f). However, both graupel and hail composites show the similar rearward shift of precipitation in the NonTOR composite.

Owing to the relationship between hydrometeor mass and K_{DP}, we expect to see this same rearward shift in the composite K_{DP} fields. Figure 14 shows that, indeed, this is the case. The NonTOR composite K_{DP} enhancement region is increased in magnitude by 0.5° km^{-1} and shifted rearward by 3.625 km compared to the TOR composite K_{DP} enhancement region. The TOR composite K_{DP} enhancement region also extends further northeast into the forward flank due to the increased rain mass in this region. The combination of the rearward shift of the NonTOR composite K_{DP} enhancement region and the separation vector orientations further from orthogonal (shown in Fig. 10) for the NonTOR simulations shows support for H1 and H2.

To discern how much of this rearward K_{DP} shift in the NonTOR composite is due to the background storm-relative wind profile compared to the winds within the storm itself (e.g., the mesocyclone), we use the size sorting toy model presented in Loeffler and Kumjian (2020). A detailed description of the toy model can be found in Loeffler and Kumjian (2020) but will be briefly explained here. The toy model is three-dimensional with a prescribed vertical wind profile and horizontally homogeneous winds. It is a steady-state model (i.e., no dependence on time) and thus captures the persistent size sorting as a result of the storm-relative winds. Only liquid (no ice) hydrometeors are used in the model and microphysical processes are ignored. A "cloud base" is located at the top of the model domain (3 km AGL) and centered in the middle (0 km, 0 km) and each grid cell is initialized with a three-parameter gamma DSD. The steady-state DSDs for every grid cell in the domain are a result of only advection by the storm-relative winds and sedimentation. The terminal velocity equation from Brandes et al. (2002) is used to determine the fall speed for each raindrop size bin. The DSDs in each grid cell are then used in the polarimetric radar forward operator described above, and more formally in the appendix, to produce the polarimetric radar variables at S band for every grid cell in the domain.

We use the average TOR and NonTOR 0–3-km storm-relative wind profiles in the toy model. The locations of the K_{DP}

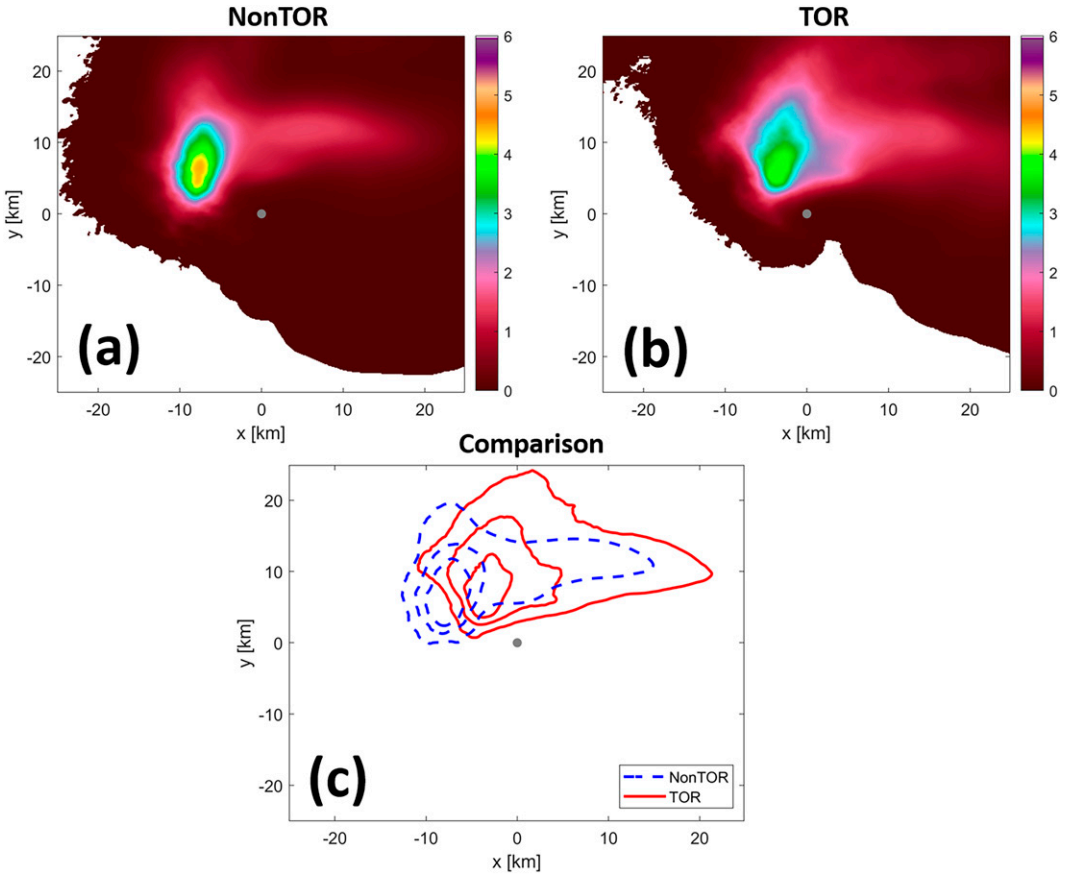

FIG. 14. Near-surface composite fields of K_{DP} (° km^{-1}) for (a) NonTOR, (b) TOR, and (c) a comparison of the two simulation types. NonTOR (blue dashed) and TOR (red solid) contours are shown for 1°, 2°, and 3° km^{-1}.

enhancement regions resulting from these toy model simulations are shown in Fig. 15. In this figure, the anchor point for the K_{DP} composites was changed to the rainwater mass mixing ratio maximum at 3 km AGL for a more direct comparison with the toy model. We see a clear westward shift in the NonTOR K_{DP} enhancement region compared to the TOR K_{DP} enhancement region. This is reflected in the separation orientation angle values, taken both relative to the 0–3-km shear vector [consistent with Loeffler and Kumjian (2020)] and relative to the simulated storm motion vector (Table 1). Once again, we see a tendency for the TOR storm-relative wind profile to produce separation orientation angles closer to orthogonal, and these orientation angles from the toy model compare favorably with those seen in the simulations. The separation distances in the toy model, however, are much smaller than those in the simulations. Additionally, there is a difference in the relative locations of the K_{DP} enhancement regions when comparing the composite fields and the toy model. In the composite fields, the NonTOR enhancement region is shifted a lesser distance rearward (0.63 km) relative to the TOR enhancement region compared to a similar relative rearward shift in the toy model (1.68 km). Considering a deeper sorting layer for these simulations would increase the residence time of the hydrometeors and, therefore, increase the magnitude of size sorting. However, for these storm-relative wind profiles, expanding the sorting layer would introduce more westerly winds into the layer and cause the mean storm-relative wind vector to be more southerly or southwesterly. This would be detrimental to producing the further rearward/westward shift that we see in the precipitation and K_{DP} enhancement regions, so it is unclear if a deeper sorting layer should be considered when assessing this size sorting signature. The enhancement regions in the simulations may also be closer to the 3 km AGL anchor point owing to melting of graupel and hail, which descend more rapidly and have decreased residence times, contributing to the rain mass and K_{DP} fields.

To test the third part of the hypothesis (H3), we analyze the NonTOR and TOR composite fields of near-surface buoyancy (Fig. 16). We have established that there is a rearward shift in the bulk of the precipitation mass for the NonTOR composite, and this is also reflected in a rearward shift in the NonTOR K_{DP} enhancement region. This precipitation is associated with several processes that contribute to negative buoyancy generation: evaporation, melting, and precipitation loading. As expected, we see a rearward shift in the NonTOR negative buoyancy region (Fig. 16c). However, this rearward shift has actually placed the negative buoyancy region farther away from the updraft in the NonTOR composite compared to the TOR composite, inconsistent with H3. These results indicate that, although the rearward shift in precipitation mass does lead to the

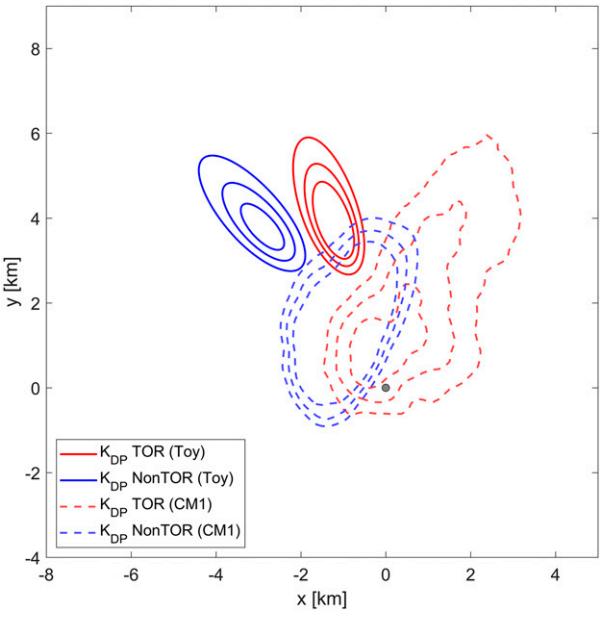

FIG. 15. Comparison of K_{DP} fields from using the average TOR and NonTOR VORTEX2 wind profiles in the size sorting toy model and the composite enhancement regions from CM1 simulations. Contours of K_{DP} values (° km^{-1}) from the toy model for NonTOR (blue solid) and TOR (red solid) are 0.08°, 0.14°, and 0.2° km^{-1} and from the CM1 simulations for NonTOR (blue dashed) are 3.75°, 4°, and 4.25° km^{-1} and TOR (red dashed) are 2.75°, 3°, and 3.25° km^{-1} at the bottom of the sorting layer. Gray dot represents the rain-generating-cell location in the toy model and the rain mass mixing ratio maximum in the composite fields.

Z_{DR}–K_{DP} separation becoming less orthogonal, this rearward shift in precipitation mass does not place negative buoyancy in closer proximity to the updraft. Thus, it appears unlikely that the area in and around the updraft is "overrun" by negatively buoyant air that is difficult to lift (e.g., Markowski et al. 2002), leading to an inability to stretch any existing vertical vorticity to tornadic strength. Therefore, if this shift in the precipitation and observed K_{DP} enhancement region plays a role in tornadogenesis or tornadogenesis failure in these simulations, it must be a different role than what we first hypothesized.

d. *Effects of precipitation distribution on baroclinic circulation generation*

Although the rearward shift in NonTOR low-level buoyancy and K_{DP} does not result in the NonTOR updraft being overrun by negatively buoyant air, this shift could potentially still play a role in tornadogenesis. This rearward shift appears to produce a stronger buoyancy gradient northeast of the updraft in the TOR composite, in a region where air parcels approaching the updraft may pass through (e.g., Rotunno and Klemp 1985; Markowski et al. 2012a; Marquis et al. 2012; Kosiba et al. 2013; Dahl et al. 2014; Dahl 2015; Coffer and Parker 2017). Parcels passing through this region along the buoyancy gradient can obtain baroclinically generated circulation as they approach the updraft, which could strengthen the low-level mesocyclone's dynamic lifting. This indicates the rearward shift in negative buoyancy for the NonTOR composite is less conducive for parcels acquiring such baroclinically generated circulation. Our new hypothesis is that the placement of the K_{DP} enhancement region and thus region of negative buoyancy in the TOR composite leads to air parcels acquiring increased baroclinically generated circulation as they approach the updraft.

We evaluate this hypothesis by using the anchored grid composite approach for each of the 42 levels in the lowest 2 km, creating a low-level composite volume for buoyancy and the wind field. We create two low-level composite volumes, one TOR and one NonTOR. As has been done in many past studies investigating the origins of mesocyclone and tornado rotation (e.g., Rotunno and Klemp 1985; Davies-Jones and Brooks 1993; Trapp and Fiedler 1995; Mashiko et al. 2009; Markowski and Richardson 2014; Mashiko 2016; Roberts et al. 2016, 2020; Roberts and Xue 2017; Tao and Tamura 2020), material circuits are used to examine the generation of circulation within each of the composite supercells (Fig. 17). The material circuits are initially 2.5-km-radius rings introduced at an altitude of 1 km in each composite storm, centered on the circulation maximum in the respective composite storms (circulation was computed about a 2.5-km-radius ring at each grid point). The circulation about each grid point is $\Gamma(x, y) = 2\pi v r_0$ where v is the average tangential wind speed about (x, y) at a radius of $r_0 = 2.5$ km. More generally, the circulation about a material circuit is $\Gamma = \oint \mathbf{v} \cdot d\mathbf{x}$, where $\mathbf{x}$ is the position vector of each parcel within the circuit.

The circuits are tracked backward in time for 40 min using the composited (steady-state) three-dimensional velocity fields. The circuits initially consist of 2000 parcels, but additional parcels are added to the circuits as the circuits are advanced backward in time in order to ensure that adjacent parcels never drift more than 25 m apart. By the time the circuits are advanced 40 min backward, they comprise a total of approximately 9600 parcels. The irregular spacing between parcel markers along the starting point of the circuits in Figs. 17a and 17b (every 500 parcel is marked) reflects along-circuit differences in the number of parcels needed to maintain the maximum 25-m

TABLE 1. Comparison of separation characteristic values between the CM1 and toy model simulations.

	TOR	NonTOR
Orientation angle relative to shear vector (toy model)	86.06°	67.03°
Orientation angle relative to storm motion (toy model)	75.68°	49.05°
Average orientation angle relative to storm motion (CM1)	84.15°	68.51°
Separation distance (toy model)	2.67 km	3.16 km
Average separation distance (CM1)	12.10 km	8.69 km

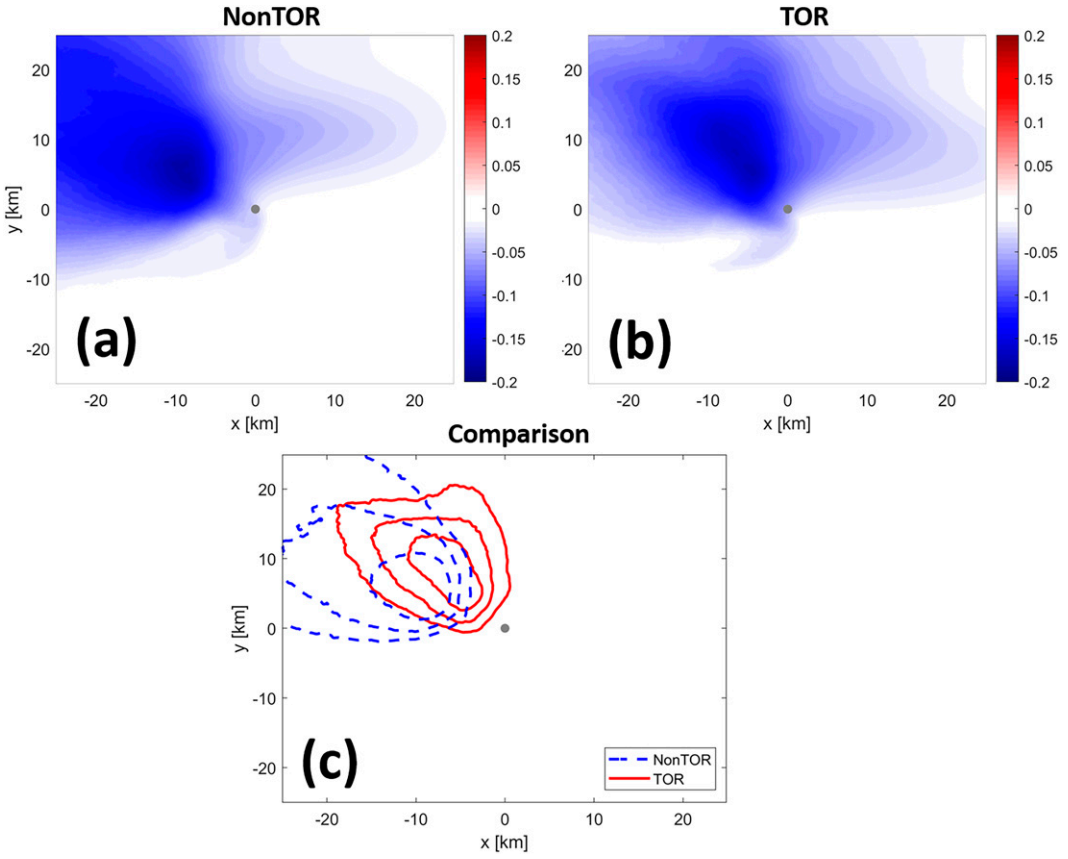

FIG. 16. As in Fig. 14, but for near-surface buoyancy (m s^{-2}). Contours are shown for −0.1, −0.125, and −0.15 m s^{-2}.

spacing along the circuits. The segments of the circuits with large spacing between parcel markers are in diffluent flow (in going backward, few parcels need to be added to the circuit); the segments of the circuits with small spacing between parcel markers are in confluent flow (in going backward, many parcels need to be added to the circuit).

In the inviscid limit, changes in circulation are governed by Bjerknes's circulation theorem, which to a good approximation, can be written as $D\Gamma/Dt = \oint B\,dz$, where B is the buoyancy, $\oint B\,dz$ is the baroclinic or solenoidal generation of circulation, and $\Gamma_{BC} = \int\oint B\,dz\,dt$ is the baroclinic circulation. Though the total circulation includes contributions from the barotropic circulation (Γ_{BT}), which is attributable to the environmental vorticity (Γ_{BT} is the circulation about the circuit when the circuit is in the environment, where $B = 0$ by definition), and the viscous circulation ($\Gamma_V = \int\oint \mathbf{F}\cdot d\mathbf{x}\,dt$, where $\mathbf{F}$ is the acceleration owing to turbulent and numerical diffusion in the simulations), our analysis is limited to the baroclinic generation of circulation, i.e., $\oint B\,dz$ and Γ_{BC}.

The viscous circulation cannot be evaluated because the subgrid-scale stress tensor and numerical diffusion were not composited. The barotropic circulation also cannot be assessed because the circuits never completely escape into the environment (i.e., the circuits never make it to a region where $B = 0$ all along the circuits). It was found to be impossible to introduce circuits into the composite storms (at least centered on the circulation maxima) without having the circuits intersect the rear-flank gust fronts, where wind speeds are vanishingly small (i.e., a stagnation zone exists). As a result, these segments of the circuits get stuck within the rear-flank regions no matter how far backward in time the trajectories are advanced (Figs. 17a,b); thus, long segments of the circuits remain stuck in the outflow and experience baroclinic circulation generation indefinitely going backward in time beyond approximately $t - 5$ min (Figs. 17c,d). This behavior is probably unrealistic and likely a consequence of assuming steady-state velocity fields. It is also futile to attempt to reconcile the circulation budgets, i.e., there is no point in comparing the time integral of $\oint B\,dz$ with the calculated Γ about the circuit because $D(\langle\mathbf{v}\rangle\cdot d\mathbf{x})/Dt \neq \int\oint\langle B\rangle dz\,dt$, where the angle brackets indicate an ensemble average, which is what we are really dealing with by analyzing the composite storms.

Focusing on the baroclinic circulation generation, the TOR composite supercell has an order of magnitude more baroclinic generation of circulation than the NonTOR composite

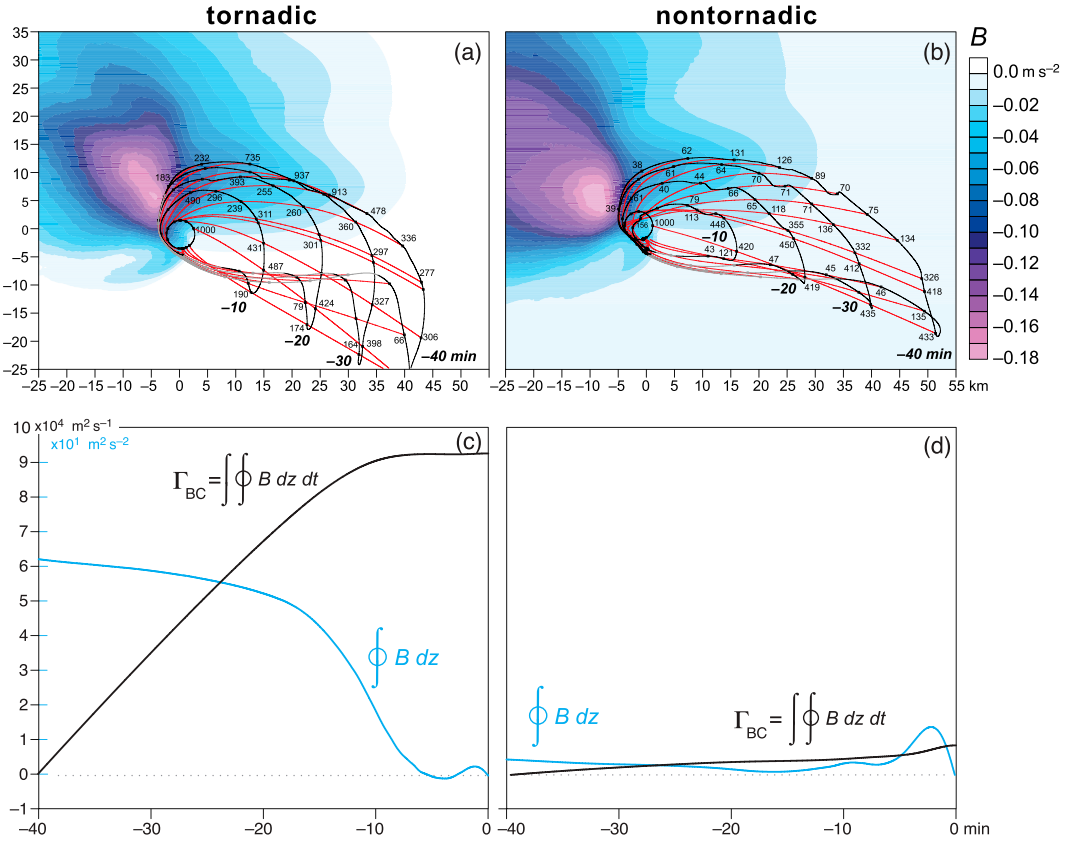

FIG. 17. (a),(b) Material circuits at 600-s intervals going backward in time to $t = -2400$ s in the TOR and NonTOR composite supercells, respectively. The circuits are overlaid atop the buoyancy fields (color shading) at the lowest grid level. Portions of the circuits that lie above the lowest scalar grid level are black and those that lie below are gray. Altitudes in meters are shown at $t = -2400$ s for every 500th parcel in the circuit. The trajectories of these parcels are also shown (red lines). At $t = 0$, the circuit has a radius of 2.5 km and is centered at the location of maximum circulation about a 2.5-km-radius ring at $z = 1$ km. (c),(d) Baroclinic circulation (Γ_{BC}; black) and baroclinic circulation generation rate ($\oint B\,dz$; cyan) about the material circuits analyzed in the TOR and NonTOR composite supercells, respectively.

supercell (Figs. 17c,d), despite having slightly less baroclinity (i.e., weaker horizontal B gradients) than the NonTOR composite supercell (Figs. 17a,b). The large differences in baroclinic circulation generation are perhaps surprising given how subtle the differences are between the B fields and horizontal projections of the trajectories in the TOR and NonTOR composite storms (the circuits in the NonTOR composite do not pass through as much negative buoyancy as those in the TOR composite; Figs. 17a,b). The vertical excursions are larger in the TOR composite as well. Thus, the circuits in the TOR composite have larger vertical projections than those in the NonTOR composite. This is consistent with larger baroclinic circulation generation, given that the depths of the baroclinity in the TOR and NonTOR composite storms are comparable (not shown). In other words, a membrane stretched over the TOR composite's material circuit would subtend a greater vertical cross section than in the NonTOR composite, and therefore would be pierced by a greater number of baroclinically generated vortex lines (as a result of Stokes's theorem, circulation is proportional to the mean normal component of the vorticity on the surface bounded by the material circuit). In summary, the rearward displacement of the K_{DP} enhancement region, and its associated negative buoyancy (see Figs. 14 and 16), in the NonTOR storms is ultimately a less favorable setup for parcels en route to the low-level mesocyclone to acquire baroclinically generated circulation. The lesser circulation (and weaker mesocyclones) at low levels, as found by Coffer et al. (2017), is associated with weaker dynamic lifting and a lower likelihood of tornadogenesis.

4. Summary and conclusions

This study investigates the potential processes that could explain the observed differences in hydrometeor size sorting signatures between TOR and NonTOR supercells and their connection to tornadogenesis. We use the Coffer et al. (2017)

ensemble of simulated supercells initialized with both TOR and NonTOR VORTEX2 composite environments. The model microphysics appears to be too aggressive in suppressing excessive size sorting, leading to a lack of a Z_{DR} arc. Although past studies have shown success with the NSSL scheme at replicating polarimetric radar signatures, future studies might consider exploring newer bulk microphysics schemes that have recently been included in CM1 (i.e., predicted particle properties (P3) scheme; Morrison and Milbrandt 2015). As a proxy, we instead use the meridional Z_H gradient along the inflow edge of the forward flank. This opens up the potential for non-polarimetric radars to assess the separation vector: using the forward flank Z_H gradient as a proxy for the Z_{DR} enhancement region and the Z_H maximum (often collocated with the K_{DP} maximum) as a proxy for the K_{DP} enhancement region.

Our initial hypotheses connecting tornadogenesis processes to the observed Z_{DR}–K_{DP} separation differences between TOR and NonTOR supercells is that a K_{DP} enhancement region placed further rearward in the supercell (H1) would lead to a more parallel (or less perpendicular) separation orientation angle in NonTOR storms (H2) and could detrimentally place the negative buoyancy region too close to the low-level updraft and circulation (H3 and H4). The separation distance in the TOR ensemble is noticeably larger than the NonTOR distances, a difference not seen in observations. However, the shift in orientation angles is consistent with observations, where the TOR separation vector orientation angles are more orthogonal to storm motion compared to NonTOR separation vector orientation angles (albeit with a smaller difference in angles compared to observations[1]), supporting H2. This is due to a storm-relative rearward shift in the NonTOR K_{DP} enhancement region compared to the TOR K_{DP} enhancement region, supporting H1. This rearward shift is also observed when the storm-relative wind profiles are used in the size sorting toy model from Loeffler and Kumjian (2020).

The environment for NonTOR supercells has stronger rearward 0–2-km storm-relative winds compared to the TOR supercell composite environment. Considering the storm-relative winds further aloft (3–6 km), the TOR composite environment contains stronger westerly/southwesterly flow compared to the NonTOR composite. This weaker flow further aloft in the NonTOR composite environment leads to weaker advection of frozen hydrometeors out into the forward flank in the NonTOR simulations compared to the TOR simulations. We see a rearward shift in the NonTOR composite graupel and hail fields and more graupel and hail mass to the northeast of the updraft in the TOR simulations. Homeyer et al. (2020) observed a midlevel Z_{DR} dipole, with a region of positive Z_{DR} values adjacent to a region of slightly negative Z_{DR} values, where the negative values indicated the presence of graupel and hail being advected out of the updraft. The negative Z_{DR} region was located more along the storm motion in TOR supercells, whereas this region was found further rearward in the NonTOR supercells. This shift in frozen hydrometeor mass aloft agrees well with the composite fields from our simulations.

As the precipitation descends, the NonTOR rearward shift is still apparent owing to stronger rearward flow, which results in the observed rearward shift in enhanced K_{DP}. This is also associated with a rearward shift in the low-level negative buoyancy; however, the NonTOR region of negative buoyancy is actually placed farther from the updraft, contrary to H3 and H4. Rather than focusing on the location of the most negatively buoyant air, this shift in low-level negative buoyancy alters the location and strength of the buoyancy gradient and, therefore, affects the production of baroclinic circulation. Material circuit analyses using the low-level composite TOR and NonTOR environments show that this shift in precipitation distribution leads to the composite TOR environment having an order of magnitude more baroclinic generation of circulation than the NonTOR composite environment. This increase in circulation enhances low-level dynamic lifting and can stretch vertical vorticity to tornadic strength.

Our findings suggest that the low-level and midlevel storm-relative winds can play a role in tornadogenesis through determining the distribution of precipitation fallout, impacting the location of associated negative buoyancy and thus altering the amount of baroclinic circulation generation. Coffer et al. (2017) analyzed the same simulations and suggest that the storm-relative winds in the 0–500 m AGL layer play the key role in tornadogenesis, with TOR supercell environments containing greater low-level streamwise vorticity and NonTOR environments containing greater low-level crosswise vorticity. Our study does not question the validity of the arguments made in Coffer et al. (2017), but rather suggests an additional mechanism simultaneously influencing tornadogenesis. Further targeted studies are needed to determine which of these processes is dominant. Nonetheless, the benefit of the mechanism regarding precipitation distribution and baroclinic circulation generation described here is that it can be assessed at the storm-scale by analyzing low-level polarimetric radar data that are routinely available to forecasters. In a situation nowcasting tornadoes, operational radar data could be utilized to assess the temporal trends of this signature in real time, with the location of negative buoyancy (determined by the K_{DP} enhancement region) relative to the mesocyclone (determined by Doppler velocities) providing an indication of how favorable the thermodynamic and kinematic fields are for generating baroclinic circulation.

Acknowledgments. The authors thank the members of the Penn State RADAR group and Yvette Richardson for their helpful comments and suggestions throughout this work. Funding for Authors Loeffler and Kumjian was provided by the VORTEX-SE program under Award NA19OAR4590222. Authors Coffer and Parker's efforts were supported by the National Oceanic and Atmospheric Administration (NOAA) Grant NA19OAR4590341 and by NSF Grant AGS-2130936. We would also like to thank three anonymous reviewers for their helpful comments and suggestions for improving this manuscript. The views of the lead author do not necessarily reflect the views of the U.S. Navy.

[1] Similar TOR and NonTOR environments in these simulations are likely to yield smaller differences than found in studies with a broader set of environments.

Data availability statement. Model input files and analysis scripts are available through the Penn State Data Commons (https://doi:10.26208/x1d1-gs56).

APPENDIX

Radar Forward Operator

To convert our model hydrometeor output fields (number concentration mixing ratio N and mass mixing ratio q) into polarimetric radar variables, we use a polarimetric radar forward operator similar to ones described in Ryzhkov et al. (2011, hereafter R11), Kumjian and Ryzhkov (2012), and Kumjian and Prat (2014). The polarimetric radar variables are calculated for an S-band wavelength (11 cm). Raindrops are divided into 0.1-mm intervals ranging from 0.05 to 7.95 mm and are oriented with a 0° mean canting angle with respect to vertical and a standard deviation of the distribution of canting angles $\sigma = 10°$.

To account for the effects of melting hail on the simulated polarimetric radar variables, we use a similar treatment to Kumjian et al. (2018, hereafter K18). Hailstones are divided into 0.1-mm bins with ice-core diameters ranging from 0.1 to 40 mm. The ice cores are assumed to be solid ice with density $\rho_{ice} = 917$ kg m^{-3}. These hailstones contain a liquid water coating determined by the maximum amount of retainable meltwater following Rasmussen and Heymsfield (1987) and Ryzhkov et al. (2013):

$$m_{w,\max} = m_8 + 0.139\,(m_i + m_{w,\text{soak}}). \tag{A1}$$

In (A1), $m_{w,\max}$ is the maximum retainable meltwater, $m_8 = 2.68 \times 10^{-4}$ kg is the mass of an 8-mm raindrop, m_i is the ice core mass, and $m_{w,\text{soak}}$ is the mass of liquid that is soaked within the stone. Because the ice cores are assumed to be solid ice, $m_{w,\text{soak}} = 0$ here.

For melting hailstones, the meltwater tends to concentrate near the equator of the stone, forming a liquid "torus" (Rasmussen et al. 1984). Because of this preferential concentration of meltwater, the overall particle (ice + liquid) axis ratio $\gamma \equiv a/b$ could differ from the ice-core axis ratio $\gamma_i \equiv a_i/b_i$, in contrast to other treatments, which assume $\gamma = \gamma_i$ (e.g., R11). The values a and b correspond to the minor and major axis, respectively. In this study, $\gamma_i = 0.7$ (e.g., Shedd et al. 2021), and γ is determined by γ_i and the liquid water mass fraction:

$$f_{\text{mw}} = \frac{m_{\text{liq}}}{m_{\text{liq}} + m_i}. \tag{A2}$$

In (A2), f_{mw} is the liquid water mass fraction and m_{liq} is the mass of liquid meltwater. The reader is referred to K18 for a detailed derivation of the overall particle axis ratio. A minimum threshold of $\gamma = 0.56$ is used here, equivalent to that of a large 8-mm raindrop. The relationship between liquid water mass fraction and ice-core size is shown in Fig. A1.

An additional modification we make is for the standard deviation of the distribution of canting angles for melting hailstones, σ_{melt} (Fig. A2). In general, σ_{melt} is assumed to vary between that of rain (σ_{rain}) and that of dry hail (σ_{dry}) depending on ice-core size, liquid water fraction, and/or axis ratios. Here, we assume $\sigma_{\text{rain}} = 10°$ and $\sigma_{\text{dry}} = 60°$ following Dawson et al. (2014) and Johnson et al. (2016). The σ_{dry} is increased compared to the 40° used in R11 and K18 to emulate greater tumbling for larger hailstones that retain less liquid meltwater. We do this with the idea of replicating the "Z_{DR} hole," a region of relatively low Z_{DR} near the updraft that disrupts the Z_{DR} arc due to larger, drier hailstones [Kumjian and Ryzhkov (2009); see also schematic in Dawson et al. (2014) for reference].

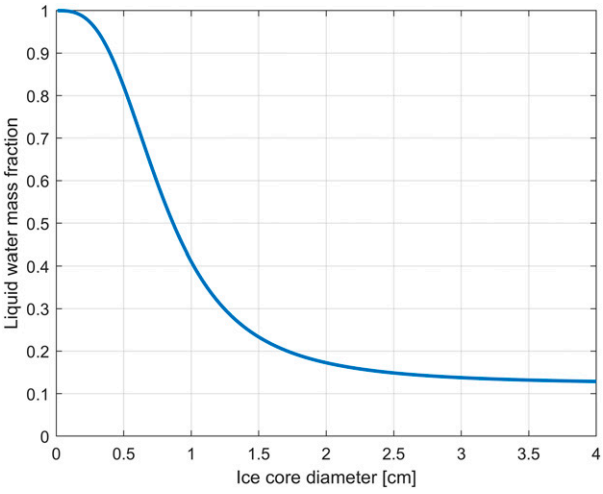

FIG. A1. Relationship between liquid water mass fraction and size of the ice core.

Both R11 and K18 present methods to determine how σ_{melt} varies between σ_{rain} and σ_{dry}. The two methods are similar except for the linear factor relating σ_{rain} and σ_{dry}: R11 use liquid water mass fraction:

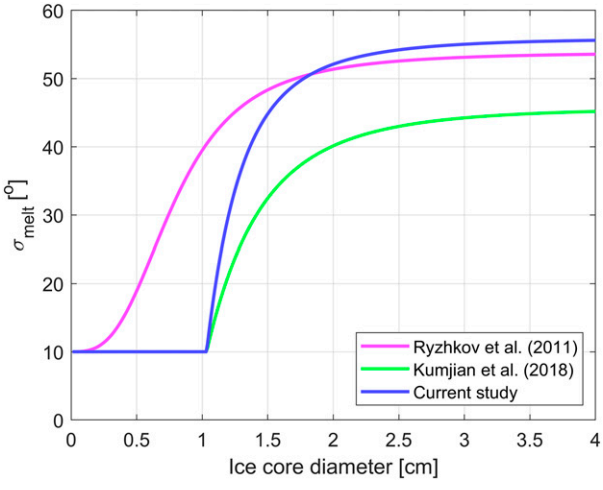

FIG. A2. Standard deviation of the distribution of canting angles as a function of ice-core size from R11, K18, and this study in magenta, green, and blue lines, respectively. This plot assumes $\sigma_{\text{rain}} = 10°$ and $\sigma_{\text{dry}} = 60°$. Note that the K18 values are identical to the values in this study for ice-core sizes less than approximately 1 cm.

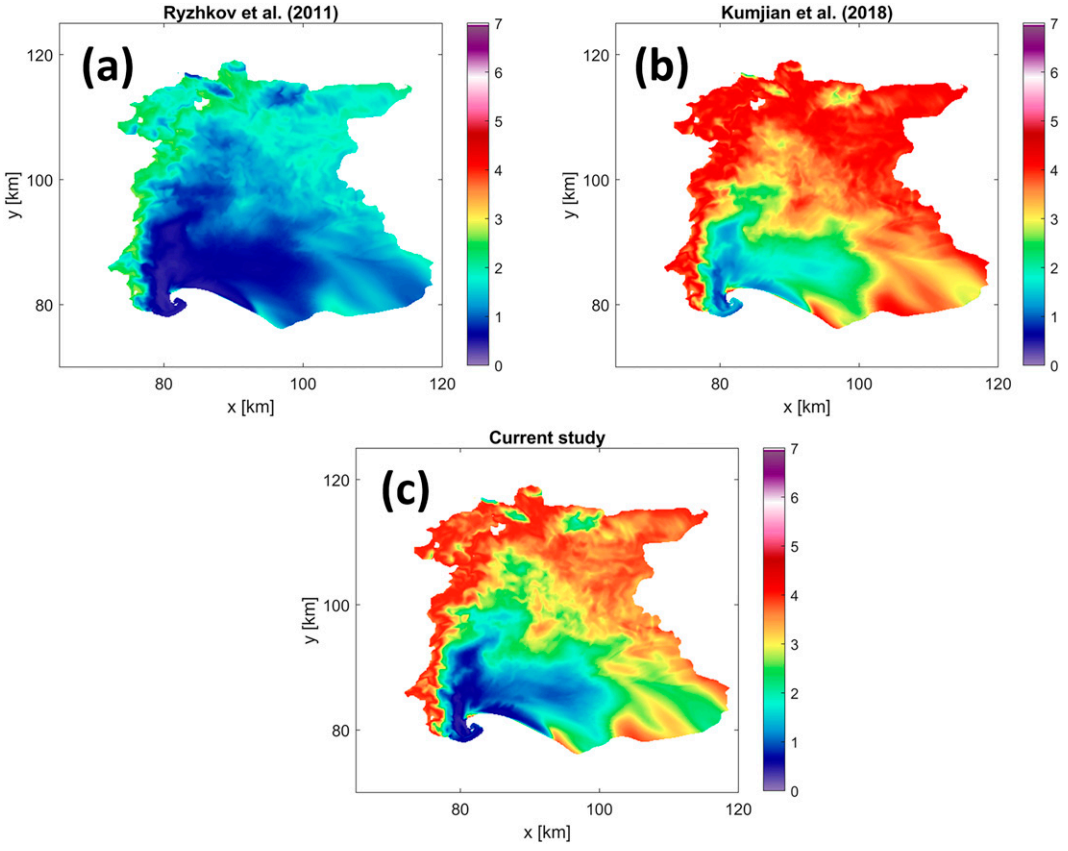

FIG. A3. Simulated near-surface hail Z_{DR} (dB) for a TOR ensemble member using parameterizations for the width of the canting angle distribution from (a) R11, (b) K18, and (c) this study. All parameterizations assume $\sigma_{rain} = 10°$ and $\sigma_{dry} = 60°$.

$$\sigma_{melt} = \sigma_{dry} + f_{mw}(\sigma_{rain} - \sigma_{dry}) \tag{A3}$$

and K18 use a ratio of aspect ratios:

$$\sigma_{melt} = \sigma_{dry} + \frac{\gamma_i - \gamma}{\max(\gamma_i - \gamma)}(\sigma_{rain} - \sigma_{dry}). \tag{A4}$$

For this study, we use a slightly different distribution by simply squaring the factor of aspect ratios in the K18 distribution:

$$\sigma_{melt} = \sigma_{dry} + \left[\frac{\gamma_i - \gamma}{\max(\gamma_i - \gamma)}\right]^2 (\sigma_{rain} - \sigma_{dry}). \tag{A5}$$

This modification allows larger hailstones to have greater σ_{melt} like those in R11, which leads to decreased Z_{DR} values, but smaller hailstones still maintain smaller σ_{melt} like those in K18, which leads to increased Z_{DR} values. An example of the resulting hail Z_{DR} fields using the three different functions for σ_{melt} assuming $\sigma_{rain} = 10°$ and $\sigma_{dry} = 60°$ are shown in Fig. A3. The R11 σ_{melt} treatment consistently produces smaller hail Z_{DR} values, resulting from the increased canting angle variability. Although small Z_{DR} values are observed close to the updraft, greater hail Z_{DR} values are associated with smaller melting hail, which has larger liquid water mass fractions and can appear to the radar similarly to a large raindrop. On the other hand, the K18 parameterization consistently produces larger hail Z_{DR} values. Our treatment produces both low Z_{DR} values (0–1 dB) near the updraft and higher Z_{DR} values on the periphery of the hail core, where hail is smaller and retains greater amounts of meltwater, consistent with observations [e.g., Fig. 4 in Kumjian (2013b)].

REFERENCES

Anderson-Frey, A. K., Y. P. Richardson, A. R. Dean, R. L. Thompson, and B. T. Smith, 2016: Investigation of near-storm environment for tornado events and warnings. *Wea. Forecasting*, **31**, 1771–1790, https://doi.org/10.1175/WAF-D-16-0046.1.

——, ——, ——, ——, and ——, 2019: Characteristics of tornado events and warnings in the southeastern United States. *Wea. Forecasting*, **34**, 1017–1034, https://doi.org/10.1175/WAF-D-18-0211.1.

Beard, K. V., 1976: Terminal velocity and shape of cloud and precipitation drops aloft. *J. Atmos. Sci.*, **33**, 851–864, https://doi.org/10.1175/1520-0469(1976)033<0851:TVASOC>2.0.CO;2.

Brandes, E. A., G. Zhang, and J. Vivekanandan, 2002: Experiments in rainfall estimation with a polarimetric radar in a subtropical environment. *J. Appl. Meteor.*, **41**, 674–685, https://doi.org/10.1175/1520-0450(2002)041<0674:EIREWA>2.0.CO;2.

Brooks, H. E., and J. Correia Jr., 2018: Long-term performance metrics for National Weather Service tornado warnings. *Wea. Forecasting*, **33**, 1501–1511, https://doi.org/10.1175/WAF-D-18-0120.1.

Brotzge, J. A., S. E. Nelson, R. L. Thompson, and B. T. Smith, 2013: Tornado probability of detection and lead time as a function of convective mode and environmental parameters. *Wea. Forecasting*, **28**, 1261–1276, https://doi.org/10.1175/WAF-D-12-00119.1.

Bryan, G. H., and J. M. Fritsch, 2002: A benchmark simulation for moist nonhydrostatic numerical models. *Mon. Wea. Rev.*, **130**, 2917–2928, https://doi.org/10.1175/1520-0493(2002)130<2917:ABSFMN>2.0.CO;2.

Coffer, B. E., and M. D. Parker, 2017: Simulated supercells in nontornadic and tornadic VORTEX2 environments. *Mon. Wea. Rev.*, **145**, 149–180, https://doi.org/10.1175/MWR-D-16-0226.1.

——, and ——, 2018: Is there a "tipping point" between simulated nontornadic and tornadic supercells in VORTEX2 environments? *Mon. Wea. Rev.*, **146**, 2667–2693, https://doi.org/10.1175/MWR-D-18-0050.1.

——, ——, J. M. L. Dahl, L. J. Wicker, and A. J. Clark, 2017: Volatility of tornadogenesis: An ensemble of simulated nontornadic and tornadic supercells in VORTEX2 environments. *Mon. Wea. Rev.*, **145**, 4605–4625, https://doi.org/10.1175/MWR-D-17-0152.1.

Coniglio, M. C., 2012: Verification of RUC 0–1-h forecasts and SPC mesoscale analyses using VORTEX2 soundings. *Wea. Forecasting*, **27**, 667–683, https://doi.org/10.1175/WAF-D-11-00096.1.

Crowe, C. C., C. J. Schultz, M. Kumjian, L. D. Carey, and W. A. Petersen, 2012: Use of dual-polarization signatures in diagnosing tornadic potential. *Electron. J. Oper. Meteor.*, **13**, 57–78, https://nwafiles.nwas.org/ej/pdf/2012-EJ5.pdf.

Dahl, J. M. L., 2015: Near-ground rotation in simulated supercells: On the robustness of the baroclinic mechanism. *Mon. Wea. Rev.*, **143**, 4929–4942, https://doi.org/10.1175/MWR-D-15-0115.1.

——, M. D. Parker, and L. J. Wicker, 2014: Imported and storm-generated near-ground vertical vorticity in a simulated supercell. *J. Atmos. Sci.*, **71**, 3027–3051, https://doi.org/10.1175/JAS-D-13-0123.1.

Davies-Jones, R., 1984: Streamwise vorticity: The origin of updraft rotation in supercell storms. *J. Atmos. Sci.*, **41**, 2991–3006, https://doi.org/10.1175/1520-0469(1984)041<2991:SVTOOU>2.0.CO;2.

——, and H. E. Brooks, 1993: Mesocyclogenesis from a theoretical perspective. *The Tornado: Its Structure, Dynamics, Prediction, and Hazards*, *Geophys. Monogr.*, Vol. 79, Amer. Geophys. Union, 105–114.

Dawson, D. T., II, E. R. Mansell, Y. Jung, L. J. Wicker, M. R. Kumjian, and M. Xue, 2014: Low-level Z_{DR} signatures in supercell forward flanks: The role of size sorting and melting of hail. *J. Atmos. Sci.*, **71**, 276–299, https://doi.org/10.1175/JAS-D-13-0118.1.

——, ——, and M. R. Kumjian, 2015: Does wind shear cause hydrometeor size sorting? *J. Atmos. Sci.*, **72**, 340–348, https://doi.org/10.1175/JAS-D-14-0084.1.

Doviak, R. J., and D. S. Zrnić, 1993: *Doppler Radar and Weather Observations*. 2nd ed. Dover Publications, 562 pp.

——, V. Bringi, A. Ryzhkov, A. Zahrai, and D. Zrnić, 2000: Considerations for polarimetric upgrades to operational WSR-88D radars. *J. Atmos. Oceanic Technol.*, **17**, 257–278, https://doi.org/10.1175/1520-0426(2000)017<0257:CFPUTO>2.0.CO;2.

Foote, G. B., and P. S. du Toit, 1969: Terminal velocity of raindrops aloft. *J. Appl. Meteor.*, **8**, 249–253, https://doi.org/10.1175/1520-0450(1969)008<0249:TVORA>2.0.CO;2.

Gallo, B. T., A. J. Clark, B. T. Smith, R. L. Thompson, I. Jirak, and S. R. Dembek, 2018: Blended probabilistic tornado forecasts: Combining climatological frequencies with NSSL–WRF ensemble forecasts. *Wea. Forecasting*, **33**, 443–460, https://doi.org/10.1175/WAF-D-17-0132.1.

Gray, K., and J. Frame, 2021: The impact of midlevel shear orientation on the longevity of and downdraft location and tornado-like vortex formation within simulated supercells. *Mon. Wea. Rev.*, **149**, 3739–3759, https://doi.org/10.1175/MWR-D-21-0085.1.

Gunn, R., and G. D. Kinzer, 1949: The terminal velocity of fall for water droplets in stagnant air. *J. Meteor.*, **6**, 243–248, https://doi.org/10.1175/1520-0469(1949)006<0243:TTVOFF>2.0.CO;2.

Homeyer, C. R., T. N. Sandmæl, C. K. Potvin, and A. M. Murphy, 2020: Distinguishing characteristics of tornadic and nontornadic supercell storms from composite mean analyses of radar observations. *Mon. Wea. Rev.*, **148**, 5015–5040, https://doi.org/10.1175/MWR-D-20-0136.1.

Johnson, M., Y. Jung, D. T. Dawson II, and M. Xue, 2016: Comparison of simulated polarimetric signatures in idealized supercell storms using two-moment bulk microphysics schemes in WRF. *Mon. Wea. Rev.*, **144**, 971–996, https://doi.org/10.1175/MWR-D-15-0233.1.

Jones, T. A., K. M. McGrath, and J. T. Snow, 2004: Association between NSSL mesocyclone detection algorithm-detected vortices and tornadoes. *Wea. Forecasting*, **19**, 872–890, https://doi.org/10.1175/1520-0434(2004)019<0872:ABNMDA>2.0.CO;2.

Jurewicz, M. L., Sr., and C. Gitro, 2014: The utility of considering dual-polarization radar signatures in the tornado warning process. *22nd U.S./Canada Great Lakes Operational Meteorology Workshop*, Ann Arbor, MI, National Weather Association.

Klees, A. M., Y. P. Richardson, P. M. Markowski, C. Weiss, J. M. Wurman, and K. K. Kosiba, 2016: Comparison of the tornadic and nontornadic supercells intercepted by VORTEX2 on 10 June 2010. *Mon. Wea. Rev.*, **144**, 3201–3231, https://doi.org/10.1175/MWR-D-15-0345.1.

Kosiba, K., J. Wurman, Y. Richardson, P. Markowski, P. Robinson, and J. Marquis, 2013: Genesis of the Goshen County, Wyoming, tornado on 5 June 2009 during VORTEX2. *Mon. Wea. Rev.*, **141**, 1157–1181, https://doi.org/10.1175/MWR-D-12-00056.1.

Kumjian, M. R., 2013a: Principles and applications of dual-polarization weather radar. Part I: Description of the polarimetric radar variables. *J. Oper. Meteor.*, **1**, 226–242, https://doi.org/10.15191/nwajom.2013.0119.

——, 2013b: Principles and applications of dual-polarization weather radar. Part II: Warm- and cold-season applications. *J. Oper. Meteor.*, **1**, 243–264, https://doi.org/10.15191/nwajom.2013.0120.

——, 2013c: Principles and applications of dual-polarization weather radar. Part III: Artifacts. *J. Oper. Meteor.*, **1**, 265–274, https://doi.org/10.15191/nwajom.2013.0121.

——, and A. V. Ryzhkov, 2008: Polarimetric signatures in supercell thunderstorms. *J. Appl. Meteor. Climatol.*, **47**, 1940–1961, https://doi.org/10.1175/2007JAMC1874.1.

——, and ——, 2009: Storm-relative helicity revealed from polarimetric radar measurements. *J. Atmos. Sci.*, **66**, 667–685, https://doi.org/10.1175/2008JAS2815.1.

——, and ——, 2012: The impact of size sorting on the polarimetric radar variables. *J. Atmos. Sci.*, **69**, 2042–2060, https://doi.org/10.1175/JAS-D-11-0125.1.

——, and O. P. Prat, 2014: The impact of raindrop collisional processes on the polarimetric radar variables. *J. Atmos. Sci.*, **71**, 3052–3067, https://doi.org/10.1175/JAS-D-13-0357.1.

——, A. P. Khain, N. Benmoshe, E. Ilotoviz, A. V. Ryzhkov, and V. T. J. Phillips, 2014: The anatomy and physics of Z_{DR} columns: Investigating a polarimetric radar signature with a spectral bin microphysical model. *J. Appl. Meteor. Climatol.*, **53**, 1820–1843, https://doi.org/10.1175/JAMC-D-13-0354.1.

——, Y. P. Richardson, T. Meyer, K. A. Kosiba, and J. Wurman, 2018: Resonance scattering effects in wet hail observed with a dual-X-band-frequency, dual-polarization Doppler on Wheels. *J. Appl. Meteor. Climatol.*, **57**, 2713–2731, https://doi.org/10.1175/JAMC-D-17-0362.1.

——, Z. J. Lebo, and A. M. Ward, 2019a: Storms producing large accumulations of small hail. *J. Appl. Meteor. Climatol.*, **58**, 341–364, https://doi.org/10.1175/JAMC-D-18-0073.1.

——, C. P. Martinkus, O. P. Prat, S. Collis, M. van Lier-Walqui, and H. C. Morrison, 2019b: A moment-based polarimetric radar forward operator for warm rain microphysics. *J. Appl. Meteor. Climatol.*, **58**, 113–130, https://doi.org/10.1175/JAMC-D-18-0121.1.

Loeffler, S. D., and M. R. Kumjian, 2018: Quantifying the separation of enhanced Z_{DR} and K_{DP} regions in nonsupercell tornadic storms. *Wea. Forecasting*, **33**, 1143–1157, https://doi.org/10.1175/WAF-D-18-0011.1.

——, and ——, 2020: Idealized model simulations to determine impacts of storm-relative winds on differential reflectivity and specific differential phase fields. *J. Geophys. Res. Atmos.*, **125**, e2020JD033870, https://doi.org/10.1029/2020JD033870.

——, ——, M. Jurewicz, and M. M. French, 2020: Differentiating between tornadic and nontornadic supercells using polarimetric radar signatures of hydrometeor size sorting. *Geophys. Res. Lett.*, **47**, e2020GL088242, https://doi.org/10.1029/2020GL088242.

Mansell, E. R., 2010: On sedimentation and advection in multimoment bulk microphysics. *J. Atmos. Sci.*, **67**, 3084–3094, https://doi.org/10.1175/2010JAS3341.1.

——, C. L. Ziegler, and E. C. Bruning, 2010: Simulated electrification of a small thunderstorm with two-moment bulk microphysics. *J. Atmos. Sci.*, **67**, 171–194, https://doi.org/10.1175/2009JAS2965.1.

Markowski, P. M., and Y. P. Richardson, 2014: The influence of environmental low-level shear and cold pools on tornadogenesis: Insights from idealized simulations. *J. Atmos. Sci.*, **71**, 243–275, https://doi.org/10.1175/JAS-D-13-0159.1.

——, and ——, 2017: Large sensitivity of near-surface vertical vorticity development to heat sink location in idealized simulations of supercell-like storms. *J. Atmos. Sci.*, **74**, 1095–1104, https://doi.org/10.1175/JAS-D-16-0372.1.

——, J. M. Straka, and E. N. Rasmussen, 2002: Direct surface thermodynamic observations within the rear-flank downdrafts of nontornadic and tornadic supercells. *Mon. Wea. Rev.*, **130**, 1692–1721, https://doi.org/10.1175/1520-0493(2002)130<1692:DSTOWT>2.0.CO;2.

——, M. Majcen, Y. Richardson, J. Marquis, and J. Wurman, 2011: Characteristics of the wind field in three nontornadic low-level mesocyclones observed by the Doppler on Wheels radars. *Electron. J. Severe Storms Meteor.*, **6** (3), https://ejssm.org/archives/wp-content/uploads/2021/09/vol6-3.pdf.

——, and Coauthors, 2012a: The pretornadic phase of the Goshen County, Wyoming, supercell of 5 June 2009 intercepted by VORTEX2. Part I: Evolution of kinematic and surface thermodynamic fields. *Mon. Wea. Rev.*, **140**, 2887–2915, https://doi.org/10.1175/MWR-D-11-00336.1.

——, and Coauthors, 2012b: The pretornadic phase of the Goshen County, Wyoming, supercell of 5 June 2009 intercepted by VORTEX2. Part II: Intensification of low-level rotation. *Mon. Wea. Rev.*, **140**, 2916–2938, https://doi.org/10.1175/MWR-D-11-00337.1.

Marquis, J., Y. Richardson, P. Markowski, D. Dowell, and J. Wurman, 2012: Tornado maintenance investigated with high-resolution dual-Doppler and EnKF analysis. *Mon. Wea. Rev.*, **140**, 3–27, https://doi.org/10.1175/MWR-D-11-00025.1.

Martinaitis, S. M., 2017: Radar observations of tornado-warned convection associated with tropical cyclones over Florida. *Wea. Forecasting*, **32**, 165–186, https://doi.org/10.1175/WAF-D-16-0105.1.

Mashiko, W., 2016: A numerical study of the 6 May 2012 Tsukuba City supercell tornado. Part II: Mechanisms of tornadogenesis. *Mon. Wea. Rev.*, **144**, 3077–3098, https://doi.org/10.1175/MWR-D-15-0122.1.

——, H. Niino, and T. Kato, 2009: Numerical simulation of tornadogenesis in an outer-rainband minisupercell of Typhoon Shanshan on 17 September 2006. *Mon. Wea. Rev.*, **137**, 4238–4260, https://doi.org/10.1175/2009MWR2959.1.

Morrison, H., and J. A. Milbrandt, 2015: Parameterization of cloud microphysics based on the prediction of bulk ice particle properties. Part I: Scheme description and idealized tests. *J. Atmos. Sci.*, **72**, 287–311, https://doi.org/10.1175/JAS-D-14-0065.1.

Murdzek, S. S., P. M. Markowski, Y. P. Richardson, and R. L. Tanamachi, 2020: Processes preventing the development of a significant tornado in a Colorado supercell on 26 May 2010. *Mon. Wea. Rev.*, **148**, 1753–1778, https://doi.org/10.1175/MWR-D-19-0288.1.

Orf, L., R. Wilhemson, B. Lee, C. Finley, and A. Houston, 2017: Evolution of a long-track violent tornado within a simulated supercell. *Bull. Amer. Meteor. Soc.*, **98**, 45–68, https://doi.org/10.1175/BAMS-D-15-00073.1.

Parker, M. D., 2014: Composite VORTEX2 supercell environments from near-storm soundings. *Mon. Wea. Rev.*, **142**, 508–529, https://doi.org/10.1175/MWR-D-13-00167.1.

Peel, S., and L. J. Wilson, 2008: Modeling the distribution of precipitation forecasts from the Canadian Ensemble Prediction System using kernel density estimation. *Wea. Forecasting*, **23**, 575–595, https://doi.org/10.1175/2007WAF2007023.1.

Rasmussen, E. N., and D. O. Blanchard, 1998: A baseline climatology of sounding-derived supercell and tornado forecast parameters. *Wea. Forecasting*, **13**, 1148–1164, https://doi.org/10.1175/1520-0434(1998)013<1148:ABCOSD>2.0.CO;2.

Rasmussen, R. M., and A. J. Heymsfield, 1987: Melting and shedding of graupel and hail. Part I: Model physics. *J. Atmos. Sci.*, **44**, 2754–2763, https://doi.org/10.1175/1520-0469(1987)044<2754:MASOGA>2.0.CO;2.

——, V. Levizzani, and H. R. Pruppacher, 1984: A wind tunnel and theoretical study on the melting behavior of atmospheric ice particles: III. Experiment and theory for spherical ice particles of radius > 500 μm. *J. Atmos. Sci.*, **41**, 381–388, https://doi.org/10.1175/1520-0469(1984)041<0381:AWTATS>2.0.CO;2.

Rauber, R. M., and S. W. Nesbitt, 2018: *Radar Meteorology: A First Course*. Wiley and Sons, 496 pp.

Roberts, B., and M. Xue, 2017: The role of surface drag in mesocyclone intensification leading to tornadogenesis within an idealized supercell simulation. *J. Atmos. Sci.*, **74**, 3055–3077, https://doi.org/10.1175/JAS-D-16-0364.1.

——, ——, A. D. Schenkman, and D. T. Dawson II, 2016: The role of surface drag in tornadogenesis within an idealized supercell simulation. *J. Atmos. Sci.*, **73**, 3371–3395, https://doi.org/10.1175/JAS-D-15-0332.1.

——, ——, and D. T. Dawson II, 2020: The effect of surface drag strength on mesocyclone intensification and tornadogenesis in idealized supercell simulations. *J. Atmos. Sci.*, **77**, 1699–1721, https://doi.org/10.1175/JAS-D-19-0109.1.

Romine, G. S., D. W. Burgess, and R. B. Wilhemson, 2008: A dual-polarization-radar-based assessment of the 8 May 2003 Oklahoma City area tornadic supercell. *Mon. Wea. Rev.*, **136**, 2849–2870, https://doi.org/10.1175/2008MWR2330.1.

Rotunno, R., and J. Klemp, 1985: On the rotation and propagation of simulated supercell thunderstorms. *J. Atmos. Sci.*, **42**, 271–292, https://doi.org/10.1175/1520-0469(1985)042<0271:OTRAPO>2.0.CO;2.

Ryzhkov, A. V., and D. S. Zrnić, 2019: *Radar Polarimetry for Weather Observations*. Springer, 486 pp.

——, M. Pinsky, A. Pokrovsky, and A. Khain, 2011: Polarimetric radar observation operator for a cloud model with spectral microphysics. *J. Appl. Meteor. Climatol.*, **50**, 873–894, https://doi.org/10.1175/2010JAMC2363.1.

——, M. R. Kumjian, S. M. Ganson, and A. P. Khain, 2013: Polarimetric radar characteristics of melting hail. Part I: Theoretical simulations using spectral microphysical modeling. *J. Appl. Meteor. Climatol.*, **52**, 2849–2870, https://doi.org/10.1175/JAMC-D-13-073.1.

Sachidananda, M., and D. S. Zrnić, 1986: Differential propagation phase shift and rainfall rate estimation. *Radio Sci.*, **21**, 235–247, https://doi.org/10.1029/RS021i002p00235.

Seliga, T. A., and V. N. Bringi, 1976: Potential use of radar differential reflectivity measurements at orthogonal polarizations for measuring precipitation. *J. Appl. Meteor.*, **15**, 69–76, https://doi.org/10.1175/1520-0450(1976)015<0069:PUORDR>2.0.CO;2.

——, and ——, 1978: Differential reflectivity and differential phase shift: Applications in radar meteorology. *Radio Sci.*, **13**, 271–275, https://doi.org/10.1029/RS013i002p00271.

Shedd, L., M. R. Kumjian, I. Giammanco, T. Brown-Giammanco, and B. R. Maiden, 2021: Hailstone shapes. *J. Atmos. Sci.*, **78**, 639–652, https://doi.org/10.1175/JAS-D-20-0250.1.

Skinner, P. S., C. C. Weiss, M. M. French, H. B. Bluestein, P. M. Markowski, and Y. P. Richardson, 2014: VORTEX2 observations of a low-level mesocyclone with multiple internal rear-flank downdraft momentum surges in the 18 May 2010 Dumas, Texas, supercell. *Mon. Wea. Rev.*, **142**, 2935–2960, https://doi.org/10.1175/MWR-D-13-00240.1.

Snyder, J. C., H. B. Bluestein, V. Venkatesh, and S. J. Frasier, 2013: Observations of polarimetric signatures in supercells by an X-band mobile Doppler radar. *Mon. Wea. Rev.*, **141**, 3–29, https://doi.org/10.1175/MWR-D-12-00068.1.

Tanamachi, R. L., H. B. Bluestein, M. Xue, W.-C. Lee, K. A. Orzel, S. J. Frasier, and R. M. Wakimoto, 2013: Near-surface vortex structure in a tornado and in a sub-tornado-strength convective-storm vortex observed by a mobile, W-band radar during VORTEX2. *Mon. Wea. Rev.*, **141**, 3661–3690, https://doi.org/10.1175/MWR-D-12-00331.1.

Tao, T., and T. Tamura, 2020: Numerical study of the 6 May 2012 Tsukuba supercell tornado: Vorticity sources responsible for tornadogenesis. *Mon. Wea. Rev.*, **148**, 1205–1228, https://doi.org/10.1175/MWR-D-19-0095.1.

Thompson, R. L., R. Edwards, J. A. Hart, K. L. Elmore, and P. Markowski, 2003: Close proximity soundings within supercell environments obtained from the Rapid Update Cycle. *Wea. Forecasting*, **18**, 1243–1261, https://doi.org/10.1175/1520-0434(2003)018<1243:CPSWSE>2.0.CO;2.

——, B. T. Smith, J. S. Grams, A. R. Dean, and C. Broyles, 2012: Convective modes for significant severe thunderstorms in the contiguous United States. Part II: Supercell and QLCS tornado environments. *Wea. Forecasting*, **27**, 1136–1154, https://doi.org/10.1175/WAF-D-11-00116.1.

Thurai, M., and V. N. Bringi, 2005: Drop axis ratios from a 2D video disdrometer. *J. Atmos. Oceanic Technol.*, **22**, 966–978, https://doi.org/10.1175/JTECH1767.1.

——, M. Szakáll, V. N. Bringi, K. V. Beard, S. K. Mitra, and S. Borrmann, 2009: Drop shapes and axis ratio distributions: Comparison between 2D video disdrometer and wind-tunnel measurements. *J. Atmos. Oceanic Technol.*, **26**, 1427–1432, https://doi.org/10.1175/2009JTECHA1244.1.

Trapp, R. J., 1999: Observations of nontornadic low-level mesocyclones and attendant tornadogenesis failure during VORTEX. *Mon. Wea. Rev.*, **127**, 1693–1705, https://doi.org/10.1175/1520-0493(1999)127<1693:OONLLM>2.0.CO;2.

——, and B. H. Fiedler, 1995: Tornado-like vortexgenesis in a simplified numerical model. *J. Atmos. Sci.*, **52**, 3757–3778, https://doi.org/10.1175/1520-0469(1995)052<3757:TLVIAS>2.0.CO;2.

——, G. J. Stumpf, and K. L. Manross, 2005: A reassessment of the percentage of tornadic mesocyclones. *Wea. Forecasting*, **20**, 680–687, https://doi.org/10.1175/WAF864.1.

Van Den Broeke, M. S., 2017: Polarimetric radar metrics related to tornado life cycles and intensity in supercell storms. *Mon. Wea. Rev.*, **145**, 3671–3686, https://doi.org/10.1175/MWR-D-16-0453.1.

——, J. M. Straka, and E. N. Rasmussen, 2008: Polarimetric radar observations at low levels during tornado life cycles in a small sample of classic southern plains supercells. *J. Appl. Meteor. Climatol.*, **47**, 1232–1247, https://doi.org/10.1175/2007JAMC1714.1.

Wakimoto, R. M., P. Stauffer, W.-C. Lee, N. T. Atkins, and J. Wurman, 2012: Finescale structure of the LaGrange, Wyoming, tornado during VORTEX2: GBVTD and photogrammetric analyses. *Mon. Wea. Rev.*, **140**, 3397–3418, https://doi.org/10.1175/MWR-D-12-00036.1.

Weiss, C. C., D. C. Dowell, J. L. Schroeder, P. S. Skinner, A. E. Reinhart, P. M. Markowski, and Y. P. Richardson, 2015: A comparison of near-surface buoyancy and baroclinicity across three VORTEX2 supercell intercepts. *Mon. Wea. Rev.*, **143**, 2736–2753, https://doi.org/10.1175/MWR-D-14-00307.1.

Wilson, M. B., and M. S. Van Den Broeke, 2022: Using the Supercell Polarimetric Observation Research Kit (SPORK) to examine a large sample of pretornadic and nontornadic supercells. *Electron. J. Severe Storms Meteor.*, **17** (2), https://ejssm.com/ojs/index.php/site/article/view/85.

Wurman, J., D. Dowell, Y. Richardson, P. Markowski, E. Rasmussen, D. Burgess, L. Wicker, and H. B. Bluestein, 2012: The second Verification of the Origins of Rotation in Tornadoes Experiment: VORTEX2. *Bull. Amer. Meteor. Soc.*, **93**, 1147–1170, https://doi.org/10.1175/BAMS-D-11-00010.1.

Ziegler, C. L., 1985: Retrieval of thermal and microphysical variables in observed convective storms. Part I: Model development and preliminary testing. *J. Atmos. Sci.*, **42**, 1487–1509, https://doi.org/10.1175/1520-0469(1985)042<1487:ROTAMV>2.0.CO;2.